



Band gap engineering of amine functionalized Ag(I)-based coordination polymers and their plasmonic Ag⁰ coupled novel visible light driven photo-redox system for selective oxidation of benzyl alcohol

Subrata Mandal ^a, Sachin P. Nanavati ^b, David J. Willock ^b, Rajakumar Ananthakrishnan ^{a,*}

^a Department of Chemistry, Environmental Materials & Analytical Chemistry Laboratory, Indian Institute of Technology, Kharagpur 721302, West Bengal, India

^b Cardiff Catalysis Institute, School of Chemistry, Cardiff University, Cardiff CF10 3AT, UK

ARTICLE INFO

Keywords:

Coordination polymer (CP)
Noble metal
Density functional theory (DFT)
Localised surface plasmon resonance (LSPR)
Highest occupied crystal orbital (HOCO)
Lowest unoccupied crystal orbital (LUCO)
Charge transfer
Benzaldehyde (BD)

ABSTRACT

We developed a one-pot synthetic route to design Ag nanoparticles (NPs) coupled mixed ligand Ag(I) coordination polymer (CP), Ag@Ag(I)-CP (40% NH₂) for photocatalysis. Initial combined (experimental and DFT) study on mixed ligand CPs demonstrates that a rational substitution of ligand L1: 1,4-benzenedicarboxylate by L2: 2-amino-1,4-benzenedicarboxylate enhances porosity and reduction of energy gap (2.9 eV) due to highest occupied crystal orbital (HOCO; + 2.4 V vs. NHE) suitable for BA oxidation selectively to benzaldehyde (BD) ((E⁰_{BA/BD} = + 1.9 V). When Ag NP (~ 6–7 nm) is *in-situ* encapsulated on CP, formed a coupled structure Ag@Ag(I)-CP (40% NH₂), which offered advantages on BA oxidation (k (O₂) = $7.4 \times 10^{-4} \text{ min}^{-1}$; yield: 19.1% BD, and k (persulfate) = $38.7 \times 10^{-4} \text{ min}^{-1}$; yield: 54.1% BD) along with significant stability, reusability and competitiveness than other Ag or precious metal NPs. The new material offers numerous possibilities for applications in oxidative organic transformations reactions. The simple synthetic strategy demonstrated in this work for the coupling of Ag(I) based coordination polymers with metal nanoparticles at the molecular scale for semiconductor like applications under visible light will accelerate extensive research in near future.

1. Introduction

Harnessing abundant solar light to trigger chemical reactions is an important aspect of photocatalysis for Green Chemistry applications. Typically, light is harvested using semiconducting materials such as TiO₂, ZnO, and CdS [1–6]. However, as an emerging new class of crystalline materials coordination polymers, and their subclass, metal organic frameworks (CPs/MOFs), have recently attracted significant attention as alternative photocatalysts [7–9]. Importantly, these materials offer opportunities to integrate both light-harvesting and catalytic components in a single solid-state platform [7–10] and their intrinsic properties such as high dispersion of active sites, pore size and topology, have identified them as promising candidates for applications in key areas such as optoelectronics [11,12], and photo-induced heterogeneous catalysis [6–8,13,14]. Recently, our group has explored new material based on coordination polymer (CP) consisting of Ag⁺ with 1,4-benzenedicarboxylate ligand (L1, bdc²⁻) as a new class of photocatalyst for the oxygen evolution reaction (OER) and organic pollutant removal. This material shows performance competitive with the classical

semiconductor based photocatalytic systems [15]. However, the CP exhibits a wide band gap of 3.7 eV. Thus, catalytic activity of the CP requires the absorption of UV light, which results in a practical limitation for photocatalytic application. Besides, the efficiency with which photogenerated conduction band (CB) electrons of the CP reduce O₂ to superoxide radicals is very poor due to the existence of competitive shallow Ag⁺ acceptor levels. During irradiation, Ag⁺ ions that are reduced to Ag⁰, can more easily leave their lattice sites. As a result, it is very hard to keep the Ag⁺-OC(O)-Ph-(O)CO⁻-Ag⁺ linked network in the CP intact and a certain level of loss of structural integrity occurs during photocatalysis which greatly impacts performance over multiple cycles [15]. Hence, in addition to the poor visible light activity, the stability of the CP is also an important concern which needs to be addressed.

2-amino-1,4-benzene dicarboxylic acid (NH₂-H₂bdc) is an organic ligand with a donor substituent (-NH₂). Some recent studies (theoretical and experimental) have demonstrated that the modification of the linker ligand in CP/MOF materials (MIL-125(Ti), UiO-66(Zr), MIL-101(Fe), and MIL-68(In)) through amine functionalization can influence the

* Corresponding author.

E-mail addresses: raja.iitchem@yahoo.com, raja@chem.iitkgp.ac.in (R. Ananthakrishnan).

<https://doi.org/10.1016/j.apcatb.2021.120821>

Received 21 May 2021; Received in revised form 4 October 2021; Accepted 12 October 2021

Available online 16 October 2021

0926-3373/© 2021 Published by Elsevier B.V.

bandgap and optical properties as summarized in Table 1. This apparently simple modification extends their application as potential visible light photocatalysts in organic transformations, CO₂ reduction, and water oxidation/treatments [16–27]. However, studies aimed at understanding how ligand modification affects the electronic structure of such materials and relating this to the changes in photocatalyst activity is rare. Indeed detailed investigation of the local structure of the linker in the photocatalyst after irradiation has not been covered in the literature. Thus, the substitution of a proportion of the bdc^{2−} (L1) ligand by NH₂-bdc^{2−} (L2) within CP, understanding the light absorption, and studies on the local structure of the linker after irradiation should lead to new materials with enhanced optical properties.

At the same time, the recent work by Liu et al. [28] and Ye et al. [29] on Ag₂O and Ag₃PO₄, respectively revealed that metallic Ag⁰ nanoparticles (NPs) on the surface of Ag₂O, and Ag₃PO₄ photocatalysts can produce materials that exhibit higher stability than their pure counterparts and also provide two additional notable features; the formation of a Schottky junction and the presence of a localized surface plasmon resonance [30], each improve the performance of Ag₃PO₄ and Ag₂O in photocatalytic experiments. Inspired by these reports, we decided to rationally tune the optical/electronic properties of the CP in a single solid platform by incorporating donor (−NH₂) substituent ligands and improve structural stability by integrating Ag NPs through an *in-situ* route to finally achieve a stable and efficient visible-light active photoredox system. Studies covering the stability of the NH₂-H₂bdc ligand based photocatalysts and the change in activity on prolonged or multiple uses in catalysis have been limited as recyclability testing is not often reported.

Utilization of a photoredox system, and its suitability, selectivity and stability on a targeted analyte, especially in organic transformation reactions is a critical issue [20,31]. In this respect selective photocatalytic oxidation typified by benzyl alcohol to benzaldehyde has been used as test reaction in this work as it is a key step in the production of versatile building blocks for the synthesis of pharmaceuticals and fine chemicals [32]. Some successful examples of catalysts for this oxidation reaction have been demonstrated recently using precious metal (Au, Pt) NPs coupled with semiconductor systems [32,33]. Ag NPs coupled with mixed ligand CP would be a much cheaper alternative if we were able to achieve selectivity and high efficiency and would also offer the possibility of applications in other oxidative organic transformation reactions.

Accordingly, in the present study, we attempted a facile one pot synthesis route (precipitation and chemical reduction through dimethyl formamide: DMF) to design a mixed ligand CP with Ag NPs encapsulated in the network structure (Ag@Ag(I)-CP (40%NH₂)). Distribution of the amine functionalized ligand in the nanostructure of the mixed ligand CP

and the intimacy of the interface between Ag NPs and mixed ligand CP in the coupled structures are identified from various microscopic and surface characterization techniques such as TEM, HRTEM, STEM, XPS, etc. To understand the significance of their counterparts, a series of mixed ligand CPs with various proportion of NH₂-bdc^{2−} was separately synthesized through the same route without using any reducing agent. Their structure and optical/electronic properties are further studied using a combined experimental and theoretical approach (DFT calculations). Finally, the photocatalytic oxidation of benzyl alcohol is used as a test reaction to evaluate the performance of the series of solids as a function of (1) the level of incorporation of the amine substituted ligand into the mixed ligand CP, (2) the deposition of Ag NPs in the mixed ligand and parent CP systems, and (3) the selection of oxidants (O₂ cf K₂S₂O₈). It is noted that K₂S₂O₈ is more easily activated by electron transfer and so significantly improves photocatalytic performance in comparison to the molecular oxygen. Under such conditions, we established that the visible light photocatalytic activity of the solids is strictly correlated to the NH₂-bdc^{2−} content, which is further enhanced upon combination of Ag NPs with the mixed ligand CP. We further demonstrated that maximum material stability is reached for the Ag NPs coupled to the mixed ligand CP compared to the mixed ligand CP alone. Based on the results, we deduced a probable mechanism that explains the photocatalytic behaviour of the coupled structure for the selective oxidation of benzyl alcohol to benzaldehyde under visible light.

2. Experimental section

2.1. Materials

AgNO₃, and 2-amino-1,4-benzenedicarboxylic acid were purchased from Sigma-Aldrich. 1,4-benzenedicarboxylic acid (H₂bdc) were obtained from Central Drug House (P) Ltd., India. Benzyl alcohol was purchased from Merck Specialties Pvt. Ltd., India. All other reagents/solvents used in this work were analytical grades (99.9%) and used without further purification.

2.2. Synthesis of Ag(I)-CP, Ag(I)-CP(x% NH₂), Ag@Ag(I)-CP, and Ag@Ag(I)-CP(x% NH₂)

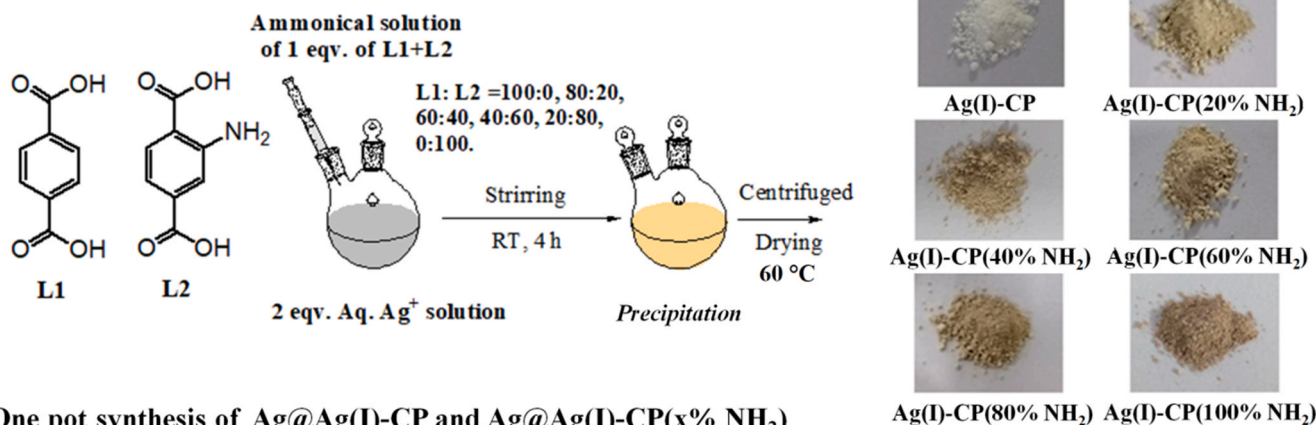
In a typical procedure (Scheme 1; top), 2 mmol of AgNO₃ was dispersed in 15 mL of deionized water, whereas 25 mL of an aqueous ammoniacal (25% NH₃) solutions of ligands (L1: 1 mmol of 1, 4 benzenedicarboxylic acid, L2: 2 amino 1, 4 benzenedicarboxylic acid) was prepared. The ligand proportions *i.e.*; L1 to L2 were set at 100: 0, 80: 20, 60: 40, 40: 60, 20: 80 and 0: 100. One mmol of that aqueous ligand (L1 + L2) solution was then gradually mixed into the *aq.* Ag⁺ solution and

Table 1

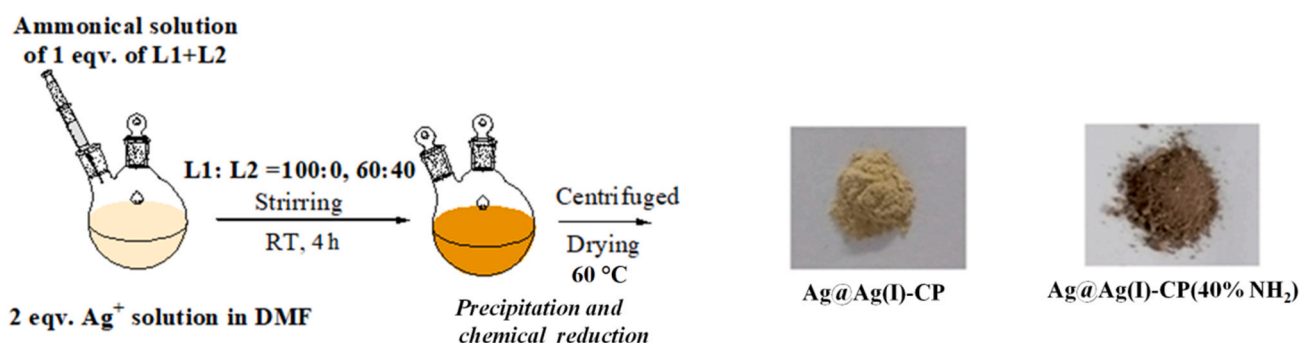
Summary of NH₂-H₂bdc (L2) based MOFs/CPs in different type of photocatalytic applications and their light absorption efficiencies and stability.

L1 based parent	L2 based photocatalyst	Band gap/ λ_{abs} range	Photocatalytic applications	Activities	Recyclability/stability
MIL 125-Ti E _g : 3.6 eV	MIL 125-Ti (NH ₂)	2.6 eV ¹⁶ 2.75 eV ¹⁹ Up to 550 nm ²⁰	NA Cr (VI) removal at $\lambda \geq 420$ nm Benzylamine oxidation ($\lambda \geq 420$ nm)	NA 91% (60 min) Conv: 73% to benzyl imines	NA 8% loss after five recycles. Three cycle
MIL-101 (Fe) λ_{abs} : 200–450 nm	NH ₂ -MIL-101(Fe)	1.32 eV ²¹ Up to 700 nm ²²	Degradation of toluene ($\lambda > 400$ nm) CO ₂ reduction ($\lambda > 420$ nm)	79% in 360 min HCOO [−] :178 μ mol 3 fold higher Superior than MIL-88B (Fe)	NA Three runs Retains Fe ³⁺ (ICP), and phase (XRD)
MIL-88B (Fe) E _g : 2.04 eV UIO-66 (Zr) E _g : 3.88–3.91 eV ^{15,16}	NH ₂ -MIL-88B (Fe) NH ₂ -UiO-66 (Zr)	Up to 750 nm ²³ 2.83 eV ²⁴ 2.76 eV ²⁵ 2.75 eV ²⁶	Cr(VI) removal ($\lambda > 420$ nm) RhB Degradation ($\lambda \geq 400$ nm) As(III) oxidation ($\lambda = 320$ –780 nm) Benzyl alcohol oxidation ($\lambda > 420$ nm)	5% (120 min) 64% (60 min) 2 time faster Conv: 11% to benzaldehyde (12 h)	Up to 4th run Retains phase (XRD), and morphology (SEM) Retains phase (XRD) after 1st cycle 3rd Cycle XRD and XPS
MIL-68 (In) E _g : 3.88 eV	NH ₂ -MIL-68(In)	2.82 eV ²⁷	Cr(VI) removal ($\lambda \geq 400$ nm)	97% in 180 min	Three cycles. Retains In (ICP), and phase (XRD, FTIR)

Synthesis of Ag(I)-CP and Ag(I)-CP(x% NH₂)



One pot synthesis of Ag@Ag(I)-CP and Ag@Ag(I)-CP(x% NH₂)



Scheme 1. Schematic illustration of the synthesis of series of Ag(I)-CP and Ag(I)-CP(x% NH₂) (top) and *in-situ* synthesis of Ag NP coupled systems: Ag@Ag(I)-CP and Ag@Ag(I)-CP(x% NH₂) (bottom).

stirred for 4 h at room temperature. The final product was separated by centrifugation and washed with water and ethanol several times to obtain Ag(I)-CP (x% NH₂). The abbreviation x% NH₂ refers to the proportion of L2 (2-amino 1, 4-benzenedicarboxylic acid) ligand with respect to total ligand (L1 + L2). Notably, when parent coordination polymer was synthesized with (100% L1) as reported earlier [15], it is abbreviated as Ag(I)-CP. Finally, all products were dried at 60 °C in vacuum. To obtain Ag@Ag(I)-CP, and Ag@Ag(I)-CP (x% NH₂), the procedure was the same, except that the solvent was changed from H₂O to DMF, as DMF could play a role as a partial reducing agent (Scheme 1; bottom). The details of the proportion of the ligand L1 and L2 for the synthesis are shown in Table S1.

2.3. Photocatalytic oxidation of benzyl alcohol

In a typical model oxidation reaction of benzyl alcohol, 25 mg of the prepared photocatalyst was placed in a 100 mL two necked cylindrical shaped pyrex glass vessel with a magnetic stirrer (300 rpm). The reaction was prepared in this vessel by the addition of 0.2 mmol of benzyl alcohol, 50 mL of CH₃CN with oxidant added separately using an O₂ balloon, 0.3 mmol of H₂O₂ (30%: w/v), and 0.22 mmol of K₂S₂O₈. Finally, the system was irradiated with a 250 W Hg lamp ($\lambda \geq 420$ nm) for 6 h (O₂) or 4 h (K₂S₂O₈). After the reaction, the catalyst was separated by centrifugation and the remaining solution was examined by HPLC and GC-MS. The concentration of remaining benzyl alcohol (BA) and products benzaldehyde (BD) in the reaction mixture was measured from the obtained areas at their respective standard retention times in the HPLC (the details of the experiment is given in the SI). The percentage conversion of BA, the selectivity and the yield for BD are measured using:

$$\text{Conversion of BA (\%)} = \frac{[\text{BA}]_0 - [\text{BA}]_t}{[\text{BA}]_0} \times 100\% \quad (1)$$

$$\text{Selectivity of BD (\%)} = \frac{[\text{BD}]_t}{[\text{BA}]_0 - [\text{BA}]_t} \times 100\% \quad (2)$$

$$\text{Yield of BD (\%)} = \text{Conversion} \times \text{Selectivity (\%)} \quad (3)$$

Where, [BA]₀ is the initial concentration of BA, [BA]_t and [BD]_t are the concentrations of BA and BD at time, *t*, respectively. For recyclability test, solid photocatalyst was washed with acetonitrile for several time (five times) and then dried at 60 °C in vacuum prior to their use in next cycle. For kinetic studies, the dispersion of catalyst and reagents was sealed in a pyrex glass vessel and kept stirring (300 rpm) for half an hour in the dark before any illumination to achieve adsorption/desorption equilibrium. The aliquots withdrawn immediately after achieving adsorption-desorption equilibrium is denoted as [BA]₀. After that reaction was carried out under illumination of a 250 W Hg lamp ($\lambda \geq 420$ nm). Further aliquots (1 mL) were then withdrawn from the reaction mixture at fixed time intervals and centrifuged to remove solid particles so that the concentration as a function of time could be obtained by analysis of those aliquots using a high performance liquid chromatography – photodiode array detector (HPLC–PDA) technique.

2.3.1. Gas chromatographic mass spectra details

Initially the solid photocatalysts were separated out from reaction mixture and the supernatant was evaporated to dryness by a rotary evaporator. The dried product was dissolved in a minimum amount of methanol, and analysed by GC-MS (Thermo Scientific Trace 1300 Gas Chromatography and ISQ single Quadrupole MS).

2.4. Characterization

FT-IR spectra were recorded using a PerkinElmer Spectrum II. Phase identification was carried out by recording XRD on a BRUKER-AXS-D8-ADVANCE diffractometer with Cu K α radiation ($\lambda = 1.5418 \text{ \AA}$) in the 2θ range of $10\text{--}90^\circ$ at a scanning rate of $0.5^\circ \text{ min}^{-1}$. Surface structures and morphologies were observed by a field-emission scanning electron microscope (NOVA NANOSEM 450) and transmission electron microscopy (TEM) and high resolution transmission electron microscopy (HRTEM). TEM was performed with JEOL JEM2010 electron microscope operating at 200 kV. The surface compositions and the oxidation states were examined by X-ray photoelectron spectroscopy (PHI 5000 Versa Probe II). BET- N_2 sorption isotherms (77 K) were performed to determine the specific surface area and the pore size distribution using Micromeritics ASAP 2020. Thermogravimetric analysis (TGA) was performed using a TG 209 F3 Tarsus (Netzsch) and the sample was heated from room temperature to 650°C at a rate of $10^\circ \text{C min}^{-1}$ under an N_2 atmosphere. Diffuse reflectance UV–vis spectra (DRS) were recorded with a Varian Cary 500 UV–vis–NIR (BaSO $_4$ background) spectrophotometer. The photoluminescence (PL) spectra of prepared solid materials were investigated and recorded by Horiba Fluorolog-3 Spectrophotometer with 380 nm of irradiation. The emission profiles of the solids were analysed using a time-correlated single-photon counting (TCSPC) picosecond spectrophotometer in ethanol at pH 7. Electron paramagnetic resonance (EPR) signal of the radicals spin-trapped by 5, 5-dimethyl-1-pyrroline-N-oxide (DMPO) was recorded using a Bruker ELEXSYS 580 X-band EPR spectrometer at room temperature (298 K) under visible-light irradiation (250 W Hg lamp; $\lambda > 420 \text{ nm}$). The settings for the EPR spectrometer were as follows: microwave frequency = 9.64 GHz.

2.5. Computational methodology

The electronic structure of parent CP and mixed ligand CP was obtained using density functional theory (DFT) as implemented in Vienna *Ab initio* Simulation Package (VASP) [34]. The projector Augmented Wave (PAW) method [35] was used to account for the interaction between the valence electrons and the core states. In the calculations, the valence electrons are expanded in terms of a plane-wave basis set with an energy cut-off (E_{cut}) of 400 eV. The valence electronic configuration of the constituent atoms are as follows: Ag: [Kr] $4d^{10} 5s^1$, O: [He] $2s^2 2p^4$, C: [He] $2s^2 2p^2$, N: [He] $2s^2 2p^3$ and H: $1s^1$. Initially, the Generalized Gradient Approximation (GGA) as parameterized by Perdew–Burke–Ernzerhof (PBE) [36] was used to approximate the exchange–correlation energy. However, for better comparison of the calculated electronic structure with experimental data, the hybrid functional of type HSE06 [37] with 25% contribution from the Hartree–Fock exact exchange energy, was employed. Dispersion corrections to account for van der Waals interactions were represented using the DFT-D3 method [38]. The convergence criteria for electronic energy and atomic forces were set to 10^{-5} eV and $10^{-3} \text{ eV \AA}^{-1}$, respectively. The Brillouin zone (BZ) was sampled with a mesh of $3 \times 3 \times 3$ k -points generated by the Monkhorst–Pack method [39]. The electronic structure has been convoluted with a Gaussian of standard deviation 0.1 eV. The electronic band structure is generated after sampling the first BZ along the high-symmetry path $G(\Gamma)\text{--}X\text{--}Y\text{--}G(\Gamma)\text{--}Z = R_2\text{--}G(\Gamma)\text{--}T_2\text{--}U_2\text{--}G(\Gamma)\text{--}V_2$, according to the recipe provided by Hinuma et al. [40]. The initial structure of the parent CP was taken from single-crystal X-ray diffraction data (CCDC 198096). The unit cell of the CP is composed of a simple monoclinic cell with two aromatic rings and a total of 36 atoms with composition $\text{Ag}_4\text{C}_{16}\text{H}_8\text{O}_8$, whose structure is shown in Fig. S1a. For the mixed ligand CP, an amine ($-\text{NH}_2$) group was substituted in the 2-position on one of the rings which results in 50% amine functionalization (Fig. S1b).

2.6. Photoelectrochemical measurements

An electrochemical workstation (Biologic SP-300) is used to measure the photocurrent and Mott–Schottky plots of the prepared sample using a three-electrode mode with 0.5 M Na_2SO_4 solution (pH = 7.0) as the electrolyte. Slurry of the sample (15 mg) were made in ethanol (1 mL) and sonicated for half an hour. Then the working electrode was prepared on Fluorine doped–Tin Oxide (FTO) glass with exposed area (A) of $1.5 \times 1.3 \text{ cm}^2$, in which 10 μL of the slurry was dropped and dried under vacuum for 1 h at 60°C . This step was repeated five times to get uniform exposure of CPs on FTO. A Pt wire was used as the counter electrode and the Ag/AgCl electrode was chosen as the reference. A 300 W Xe lamp was used as the light source (Batsol Class AAA solar simulator; Model no: PEC-L01) to measure the photocurrent response with 1 sun simulated light illumination (AM 1.5G, 100 mW cm^{-2}). Photocurrent density vs. time plot was measured at 0.0 V vs. Ag/AgCl. Light was turned on and again off for 2–3 min approximately in each cycle. In addition, the Mott–Schottky and EIS measurements were performed in the dark. For the Mott–Schottky plot, the potential range was set from -1.0 to $+0.4 \text{ V}$ (vs. Ag/AgCl). The frequency range was 100–2000 Hz, and the sinus amplitude was 0.025 V.

3. Results and discussion

3.1. Structural and surface characterizations

3.1.1. PXRD and FTIR

PXRD measurements were made for Ag(I)-CP ($x\%$ NH_2) materials with $x = 0, 20, 40, 60, 80, 100$. As shown in Fig. 1a, the diffraction peak positions for Ag(I)-CP (0, 20, 40, 60%- NH_2) materials are well matched with the simulated pattern of the monoclinic phase of $\text{Ag}_2(\text{C}_8\text{H}_4\text{O}_4)$ (CCDC 198096), meaning that all of these materials crystallize in the same topological structure as parent CP. As the proportion of L2 ($\text{NH}_2\text{--}bdc^{2-}$) increases from 40% to 60% the structure loses crystallinity and becomes more amorphous in nature as evidenced by broader PXRD peaks of materials with higher proportions of L2. A new peak at $2\theta = 16.1^\circ$ was observed for the CP containing 80% L2 and is more prominent at 100% L2, confirming that CP crystallizes into a new phase when formed solely with L2. These results indicate that substitution of L1 by L2 in the parent CP structure is limited to a maximum L2 level somewhere between 40% and 60%. In our work, we considered the discussion up to 40% amine functionalization to be relevant to mixed linker materials with the parent CP crystal structure. As the amount of L2 incorporated in the materials in this range is increased the diffraction peaks shift to lower angles as highlighted by Fig. 1b, showing this effect in the 2θ range $11\text{--}15^\circ$ and in Table 2. This data has been used to calculate the lattice parameters, cell volume and (100) lattice spacing. The experimental data shows that Ag(I)-CP (20, 40% NH_2) has a cell volume 10% greater than the Ag(I)-CP material. Such an expansion could be caused by the steric effects of the L2 ligand or the retention of solvent molecules in the pore [41]. To identify most likely reason in this case additional analysis has been carried out including FTIR spectra and TG analysis of the series of CPs as discussed in the next section. In addition, a theoretical model of the mixed linker CP has been constructed and the cell volume optimised without the inclusion of solvent so that the steric effect of amine functionalisation can be assessed.

In the theoretical model, we have attached one $-\text{NH}_2$ group to one aromatic ring (out of two) in the unit cell, thus giving a comparable 50% amine functionalization as shown in Fig. S1. The use of supercells containing more independent linker molecules was prohibited by the computational cost of the hybrid DFT calculations required for accurate band structure calculations. The bulk modulus of the system calculated using Birch–Murnaghan equation of states within GGA–PBE was 46.32 GPa (Fig. S2). The equilibrium lattice parameters are shown in Table S2. It is noted that the calculated volume of the unit cell after 50% L2 incorporation was reduced by 0.87% as compared to the parent CP.

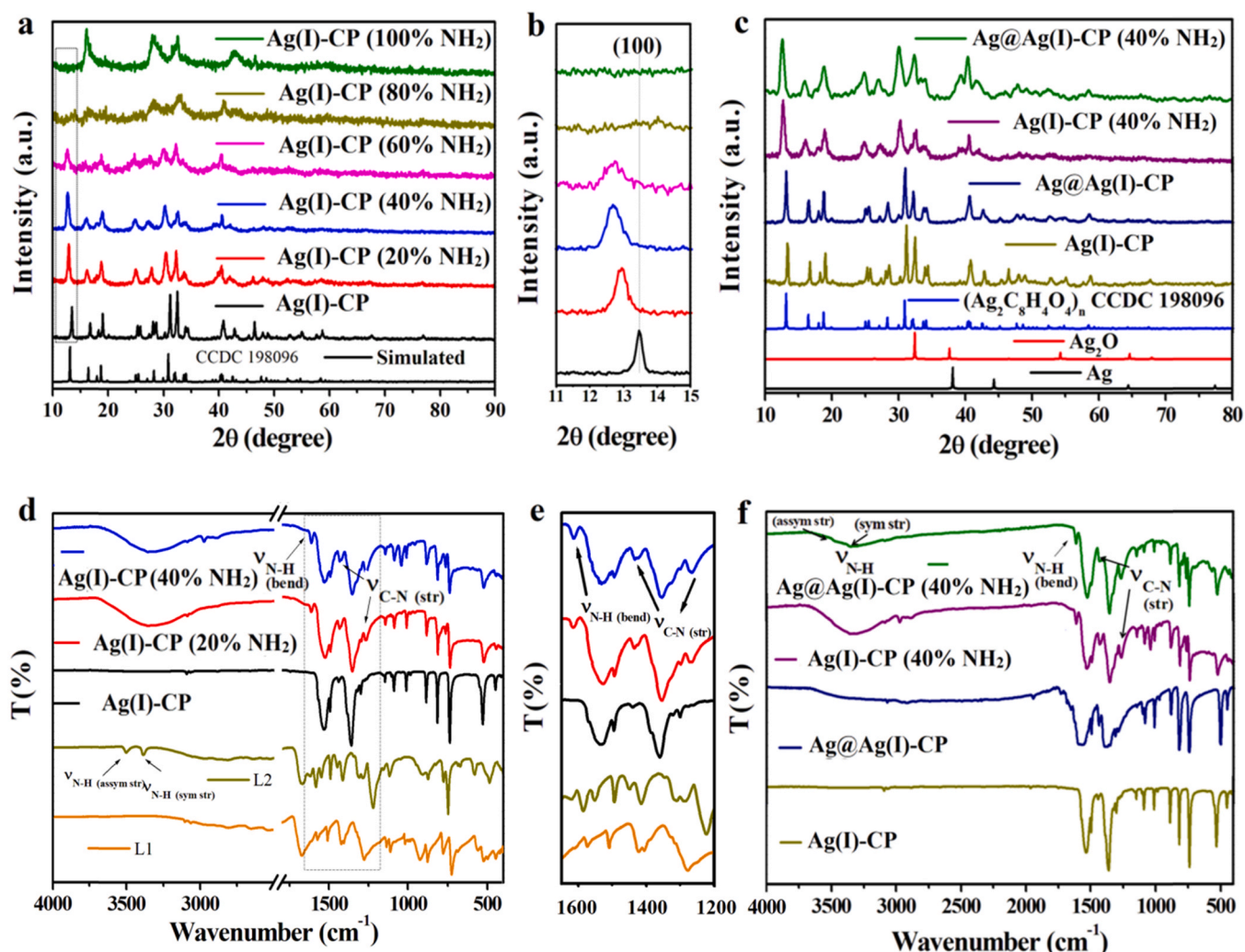


Fig. 1. (a) PXRD patterns and (b) high-resolution XRD patterns of the selected area (11–15°) of the mixed ligand CPs with their parent species, and (c) comparison of the PXRD patterns with Ag@Ag(I)-CP (40% NH₂), and Ag@Ag(I)-CP. (d and e) FTIR spectra of mixed ligand CPs with their parent species, L1, and L2 at (d) 4000–400 cm⁻¹, and (e) 1650–1200 cm⁻¹, and (f) comparison of FTIR spectra with Ag@Ag(I)-CP (40% NH₂), and Ag@Ag(I)-CP.

Table 2

Lattice parameters for Ag(I)-CP (x% NH₂) calculated from the PXRD data.

Sample name	a (Å)	b (Å)	c (Å)	Cell vol. (Å ³)	d ₍₁₀₀₎ (Å)	(2θ)
Ag(I)-CP	7.08	8.84	6.23	361.79	6.57	13.47
Ag(I)-CP(20% NH ₂)	7.30	9.23	6.22	396.77	6.85	12.90
Ag(I)-CP(40% NH ₂)	7.33	9.20	6.23	399.41	6.96	12.70

This may indicate that the experimentally observed expansion of the unit cell on aniline functionalization of the linker is to do with increased retention of solvent in the pore space of the mixed ligand CP rather than the steric requirements of the amine group. Furthermore, a tendency for a small decrease in the Ag-O bond lengths is observed (Fig. S1 and Table S2). The length of Ag-O bond connected to bdc²⁻ ligand (L1) is about 2.32–2.33 Å. When this L1 is functionalized by the -NH₂ group the Ag-O bond length connected to the NH₂-bdc²⁻ (L2) decreases to 2.30–2.31 Å, indicating that electron donation from the amine group into the aromatic system of the ligand increases the bond strength to the Ag⁺ cation [41]. The phase purity of the sample Ag@Ag(I)-CP and Ag@Ag(I)-CP (40% NH₂) synthesized in presence of DMF was also characterized by PXRD. The results as depicted in Fig. 1c clearly shows

the same diffraction pattern as indexed earlier with the binuclear monoclinic species (CCDC 198096). The simulated pattern of Ag⁰ and Ag₂O are also included for comparison. Note that there are no peaks of cubic Ag⁰ for the Ag(I)-CPs materials at the expected 2θ values. However, the absence of the characteristic peak of Ag⁰ is very common due to small crystallite size expected if silver is phase separated in Ag(I)-CP samples [14].

ATR-FTIR spectra recorded for the samples are shown in Fig. 1d and Fig. S3a. Note that, unlike the parent CP: Ag(I)-CP, ATR-FTIR spectra of the mixed ligand material show a broad range of absorptions in the region of 3000–3600 cm⁻¹ characteristic of the stretching modes of -OH groups. This indicates that for Ag(I)-CP (x% NH₂); x = 20, 40%, the amine group in the ligand facilitates the retention of solvent through hydrogen bonding interactions with adsorbed water or solvent molecules. Accordingly, for the Ag(I)-CP (x% NH₂); x = 20, 40% samples, the typical double peaks at 3470 cm⁻¹ and 3357 cm⁻¹ for asymmetric and symmetric N-H stretching vibration of the amine groups, respectively (Fig. S3b) are not obvious as they are obscured by vibrational modes associated with water. However, in the lower frequency region (Fig. 1e) the peaks centred at 1617 and 1492 cm⁻¹ correspond to the N-H bending vibrations and the peak centre at 1270 and 1440 cm⁻¹ correspond to the characteristic C-N stretching of aromatic amines [42,43] of the NH₂-bdc²⁻ moiety can be clearly seen. Note that these features are not present for spectra of the parent CP: Ag(I)-CP. This indicates that

$\text{NH}_2\text{-bdc}^{2-}$ linker is present in the Ag(I)-CP ($x\%$ NH_2) structures. Additionally, several measurements have been carried out to confirm the presence of the L2 ligand including UV–vis, XPS and EDX mapping as discussed latter of this section. Due to the presence of water or solvent content in the pore of mixed ligand CP a significant loss of crystallinity was observed in XRD pattern of the Ag(I)-CP ($x\%$ NH_2); $x = 20, 40\%$. In addition, the result also confirms solvent retention as the explanation for the increase of the cell volume and lattice parameters of the mixed ligand CP compared to the parent CP. Notably, the sample Ag@Ag(I)-CP and $\text{Ag@Ag(I)-CP}(40\% \text{ NH}_2)$ both exhibited characteristics of vibrational bands of functional groups -C=O owing to the presence of L1 ligand (Fig. 1f). An additional vibrational modes of N-H (stretching and bending), C-N (stretching) of the L2 unit were obtained for the $\text{Ag@Ag(I)-CP}(40\% \text{ NH}_2)$ sample. The result indicates that there was no alternation of the mode of functional group (-NH_2) of L2 in the sample when the reaction was carried out in the DMF.

3.1.2. BET surface area and porosity

The porosity of all the samples was measured by N_2 adsorption-desorption experiments with the results shown in Fig. 2a. All the samples exhibited a type IV isotherm [44] as at a high relative pressure (P/P_0) typical hysteresis loops are observed, characteristic of the mesoporous structure of the products. The pore volume and pore diameters of the CPs show a small increase with increasing amine content, (Table S3 and Fig. 2b) indicating the formation of mesopores. Mesopores may form by the agglomeration of particles resulting from the increase in the number interacting sites on the external surface of the CP [42,45]. The BET surface area and pore volume of the samples are shown in Table S3. Parent CP: Ag(I)-CP has a measured surface area of $29 \text{ m}^2 \text{ g}^{-1}$, the BET surface areas of Ag(I)-CP (20, 40% NH_2) are determined to be 32, $37 \text{ m}^2 \text{ g}^{-1}$, respectively. However, when DMF is used for the synthesis the surface area of the sample Ag@Ag(I)-CP and Ag@Ag(I)-CP (40% NH_2) is reduced to 23, $14 \text{ m}^2/\text{g}$, respectively. This consequent change in the surface property of the mixed ligand CPs alone and reduction of the surface area in the sample synthesized in presence of DMF are further clarified from the microscopic techniques.

3.1.3. Morphology

The FESEM images of the Ag(I)-CP (0, 20, 40% NH_2) are given in Fig. S4a–c and show that the parent CP: Ag(I)-CP crystallizes into micro-nano size rod like structures. In contrast, Ag(I)-CP (20, 40% NH_2) has a two-dimensional sheet like morphology showing that there is a change of crystal habit when L2 is introduced. This change in morphology may be induced by the N-H-O (hydrogen bonding) interaction of the amine unit of the ligand L2 either through carboxylate oxygen (interlayer) or through adsorbed water molecules as evident from the theoretical (Fig. S1) and FTIR studies (Fig. 1c), respectively. The ratio of Ag and N

obtained from energy-dispersive X-ray (EDX) analysis (Fig. S4d–i) was quantified for each sample as shown in Table S4. The results show that the percentage of N with respect to Ag in Ag(I)-CP (20% NH_2) and $\text{Ag(I)-CP}(40\% \text{ NH}_2)$ were 12%, and 21% which are close to the theoretical values of 10% and 20%, respectively. These values are as expected from the theoretical estimation during synthesis suggesting a good degree of incorporation of the amine substituted ligand into the mixed ligand CP materials. Furthermore, the EDX mapping images in Fig. S4e and h show uniform distribution of N and thereby of the 2-amino-1,4-benzenedicarboxylate linker consistent with L2 being randomly distributed throughout the mixed ligand CP. From the above studies it can be inferred that the amine functional groups do not coordinate with metal ions to form a new phase but rather sit in the pore space of the CP, interacting non-covalently with water molecules and free carboxylate groups that have not been incorporated into the CP network and that this results in two-dimensional growth of the very small crystallites while maintaining a porous structure [45–47]. To investigate the morphology and surface of the sample synthesized in presence of DMF microscopic techniques were employed. The FESEM and TEM image of the sample (Ag@Ag(I)-CP) shown in Fig. 3a and b, and Fig. S5a clearly show the presence of one-dimensional quasi rod-shaped Ag(I)-CP crystallites and these are assembled through their side edges to form into a bundle like structure.

The electron diffraction pattern of the selected area further demonstrates that the dense particles in the CP are polycrystalline and the SAED pattern can be indexed to the (110) and (200) planes of cubic Ag^0 (Fig. 3c) [48,49]. Furthermore, high resolution TEM (HRTEM) images presented in Fig. 3d–e indicate that these ultrafine silver nanoparticles on the Ag(I)-CP are spherical with an average size of $\sim 5 \text{ nm}$ as estimated from the particle size distribution (Fig. S6a). Besides, a clear contrast was observed between the boundary of the coordination polymer (Ag(I)-CP) and the ultrafine particles and a strong intimate interface is formed between these two phases. The inter-planar distance is 0.2 nm (Fig. 3e), which correlates with the (200) plane of Ag^0 . Note that deposition of metallic Ag^0 in Ag(I)-CP (40% NH_2) is also visible in FESEM and TEM (Fig. 4a and b and Fig. S5c). However, the particles are more clearly resolved in the HRTEM image (Fig. 4c). The size of the particles is around $\sim 6\text{--}7 \text{ nm}$ (histogram in Fig. S6b) here, which is slightly larger than that of particles observed in the case of the Ag@Ag(I)-CP . Note that Ag^0 NPs, encapsulated on the coordination polymer sheet facilitates a strong interface formation (Fig. 4c), which is an essential factor for the photo induced charge transfer process. The interplanar distances are measured to be 0.24 nm (Fig. 4c), which correlates with the (111) plane and the SAED pattern (Fig. 4d) indexed to the (110) (200) plane of Ag^0 [48,50]. Elemental mapping (Fig. 3f–i, and Fig. 4e–i) and EDX spectra (Fig. S5b and d) of both the coupled structures further confirmed that there was no alteration of the random

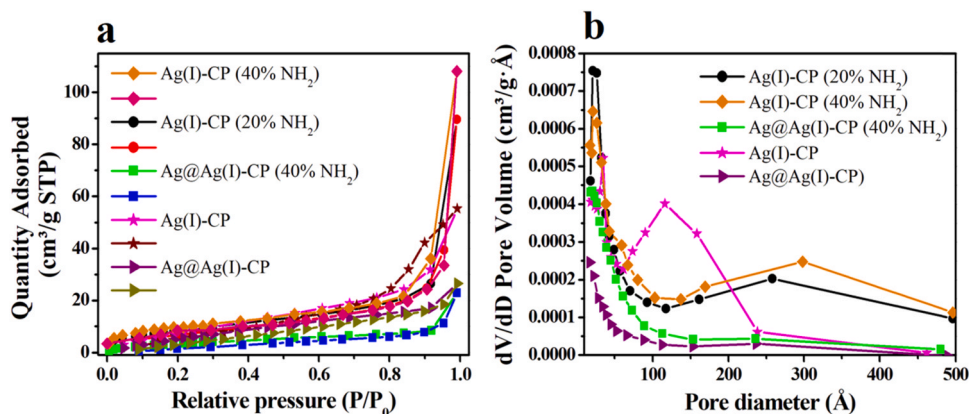


Fig. 2. (a) Nitrogen sorption isotherms, and (b) pore size distributions measured for the Ag(I)-CP , Ag(I)-CP (20% NH_2), Ag(I)-CP (40% NH_2), Ag@Ag(I)-CP , and Ag@Ag(I)-CP (40% NH_2).

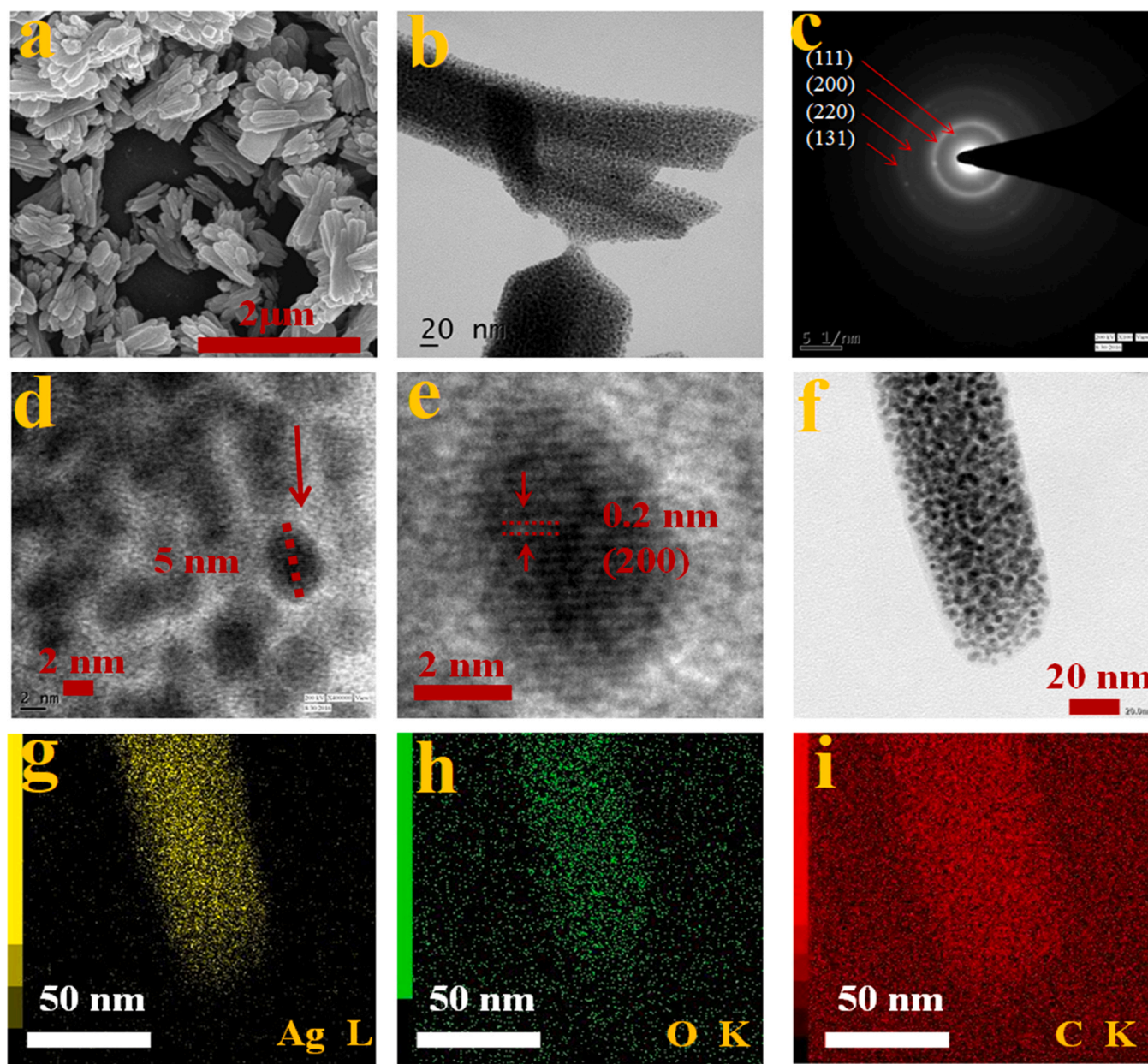


Fig. 3. (a) FESEM (b) TEM images of Ag@Ag(I)-CP, (c) SAED pattern and (d-e) HRTEM images of Ag NPs in the structure, and (f) STEM and (g-i) STEM-EDS elemental mapping images of Ag@Ag(I)-CP, showing the distribution of C red, O green, Ag yellow.

distribution of the organic moiety in the Ag(I)-CP, and Ag(I)-CP(40% NH₂) during *in-situ* formation of Ag⁰ nanoparticles.

3.1.4. XPS study

The surface chemical composition of the Ag(I)-CP (40% NH₂), and Ag@Ag(I)-CP (40% NH₂) were examined via XPS (Fig. S7). The high-resolution spectrum shown in Fig. 5a for these two solids was fitted based on the binding energy values of Ag 3d_{5/2} and Ag 3d_{3/2} at ~366.9 eV and ~372.9 eV, respectively which correspond to the Ag⁺ for Ag-O clusters [15], and binding energy values at ~367.9 eV and ~374.0 eV corresponding to Ag⁰. The XPS signals from metallic Ag⁰ make a much greater contribution for the Ag@Ag(I)-CP (40% NH₂) sample than for Ag(I)-CP (40% NH₂).

In the N 1s region of the spectrum (Fig. 5b) a peak at 399.2 eV is obtained for the Ag(I)-CP (40% NH₂), and Ag@Ag(I)-CP (40% NH₂) which was not observed in XPS measurements on Ag(I)-CP [15]. This can be attributed to uncoordinated amine groups present in the Ag(I)-CP

(40% NH₂), and Ag@Ag(I)-CP (40%-NH₂) and both materials show a shoulder feature for coordinated amine [26]. The C 1s spectrum is deconvoluted into four peaks at 283.3 eV, 284.4 eV, 286.7 eV, and 287.6 eV (Fig. 5c), which correspond to the C-C, C-N/C-O, C=C, and C=O environments of L1 and L2 in Ag(I)-CP(40% NH₂) and Ag@Ag(I)-CP(40% NH₂), respectively. The O 1s spectrum (Fig. 5d) of both materials can be fitted to three peaks. The peak at 532.7 eV is ascribed to the OH of coordinate-free carboxylic group [26]. The peaks at the binding energies of 529.9 eV, and 531.5 eV can be attributed to the lattice oxygen of the Ag-O node, and C=O/C-O of coordinated carboxylate group in the organic linker, respectively. In addition, the atomic % of Ag⁰ with respect to total silver in Ag@Ag(I)-CP (40% NH₂) is also obtained from the XPS study as shown in Table S5.

3.1.5. Quantitative analysis of the ligand (L2) and Ag⁰ in the samples

A quantitative estimation of L2 in the mixed ligand Ag(I)-CPs was carried out by disassembling the framework using 0.1 M NaOH [17,43],

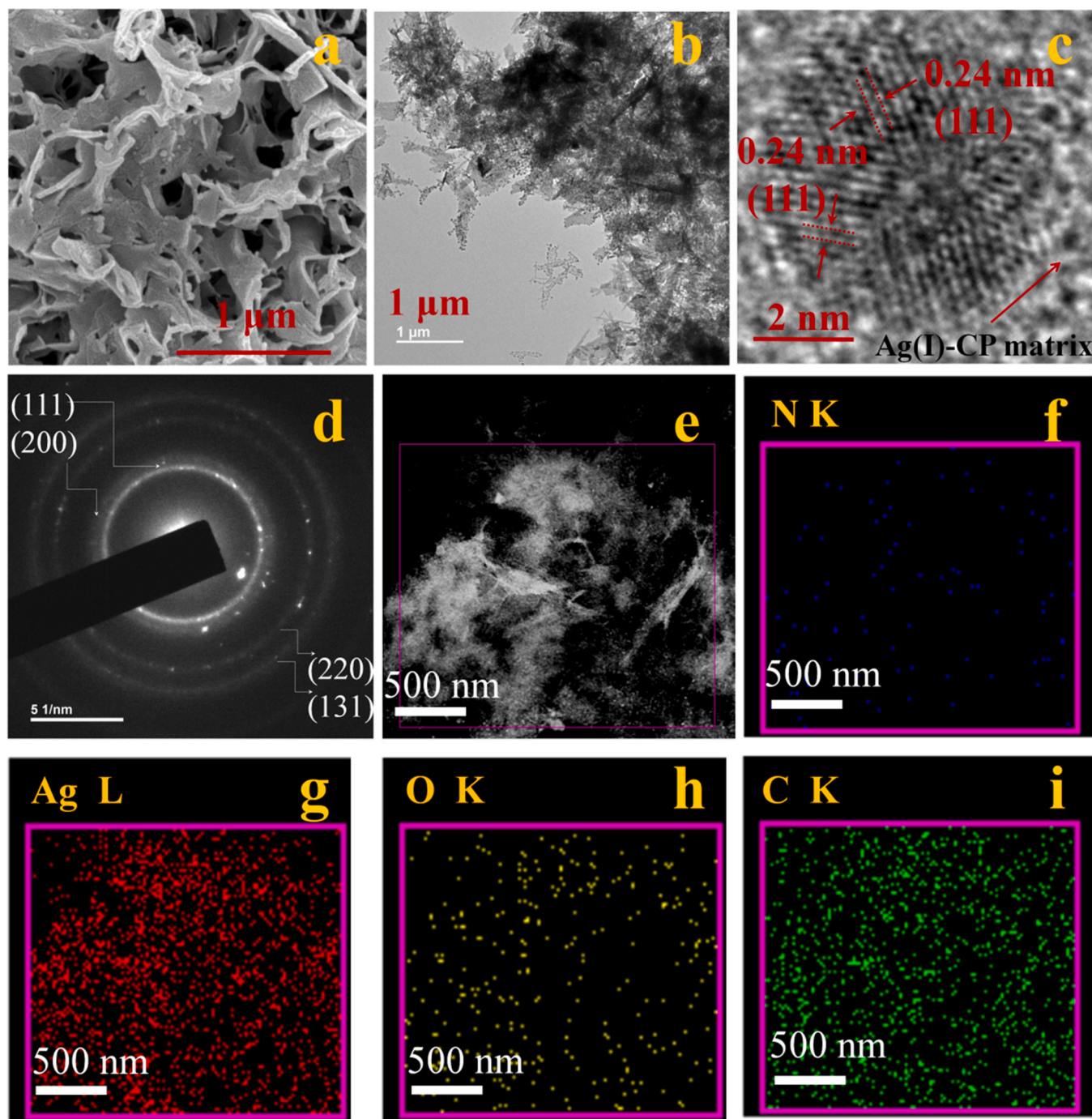


Fig. 4. (a) FESEM (b) TEM images of Ag@Ag(I)-CP (40% NH_2), (c) HRTEM image and (d) SAED pattern of Ag NPs, (e) HAADF-STEM and (f–i) EDX elemental mapping images of Ag@Ag(I)-CP (40% NH_2), showing the distribution of C green, O yellow, N blue, and Ag red.

and details of the experiment is presented in SI (Scheme S1, and Fig. S8). Fig. 6a shows the UV–visible absorption spectra of the transparent solutions recorded after digestion. The concentration of L2 in the mixed ligand CPs can be determined by measuring the absorbance of the solutions and interpolating the absorbance at 329 nm (characteristic λ_{max} of L2) from the calibration curve (inset in Fig. 6a and Fig. S9). Table S6 shows calculated L2 content in the mixed-ligand Ag(I)-CPs (detailed calculation is shown in the SI). The values of L2 content for Ag(I)-CP (20% NH_2), and Ag(I)-CP (40% NH_2) obtained by spectroscopic methods are 20.20% (± 0.20) and 40.53% (± 0.60), respectively, which are in satisfactory agreement with the expected L2: L1 ratio used in the synthesis mixtures [17]. This means that L1 and L2 are equally likely to

be incorporated into the crystalline product during synthesis. In addition, a qualitative study of the ligands (L1, and L2) after disassembling the CPs was also carried out by ^1H NMR (Scheme S1). Fig. S10 show the ^1H NMR spectra (normalized in Fig. 6b), obtained from the digestion solutions of all samples in the series. As expected from the UV–visible data, when going through the series from Ag(I)-CP (20% NH_2) to Ag(I)-CP (40% NH_2), the L2 proton signals ($3 \times ^1\text{H}$: H2, H3, H4, Fig. 6b right) systematically increases in intensity while the (L1) proton signal ($4 \times ^1\text{H}$: H1, Fig. 6b left) decreases. This result confirms that L2 substitutes for L1 to an increasing extent throughout the series. Beside NMR and UV–visible spectroscopy, TG analysis of the samples was carried out. The ratio of wt% the total ligand content (L1 + L2) and the metal (Ag^+

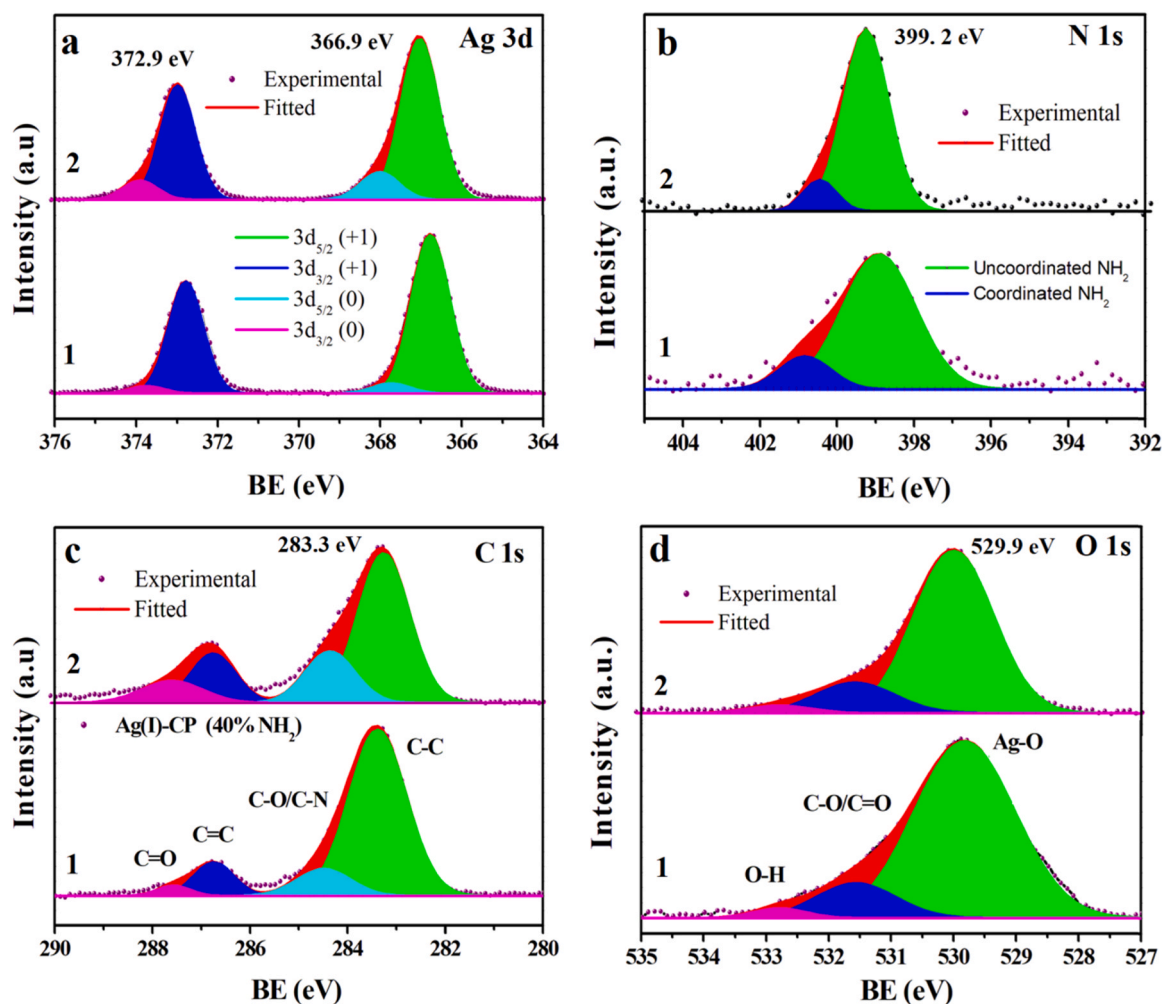


Fig. 5. High resolution XPS spectra of (a) Ag 3d, (b) N 1s, (c) C 1s, and (d) O 1s of (1) Ag(I)-CP (40% NH₂) and (2) Ag@Ag(I)-CP (40% NH₂).

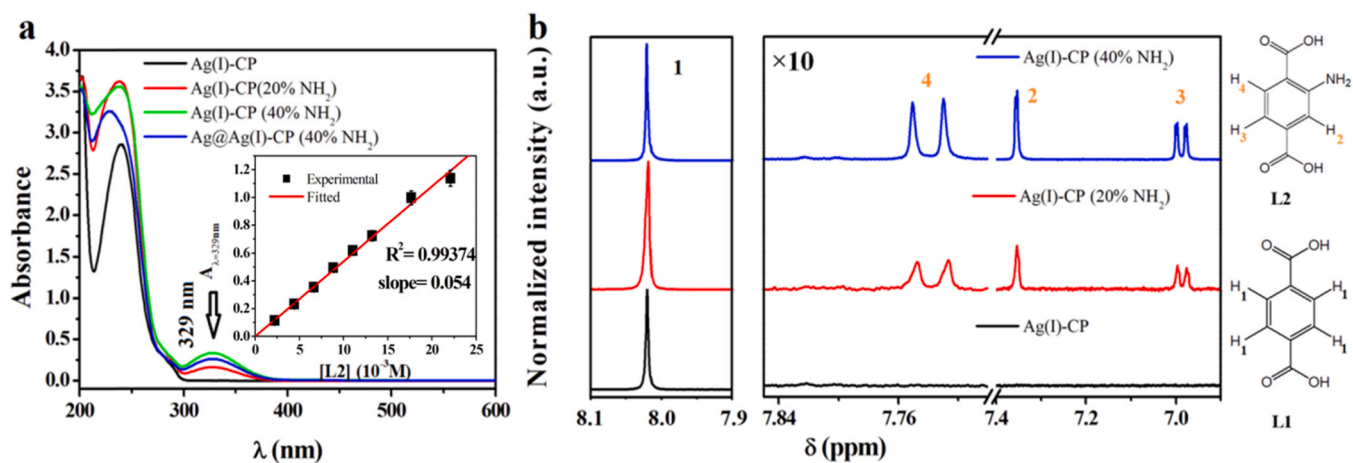


Fig. 6. (a) UV-vis absorbance spectra of the transparent solution after disassembling the solid samples with 2 mL of 0.1 M aqueous NaOH solution for 24 h. The inset shows the calibration curve obtained by plotting the absorbance (A_{329nm}) of a standard solution of 2-amino-1, 4-benzenedicarboxylic acid (L2) against concentration, and (b) Normalized ¹H NMR spectra of the solid obtained after neutralization by 0.2 M HCl from the digested CPs in DMSO (d₆): proton signal (1) associated with L1 and (2–4) signals associated with L2. Signals in the panel (b) are actually multiplied by a factor of 10 for easy visual comparison of the signal intensities.

and Ag⁰) in each sample (Fig. S11) are then evaluated from their respective TG curve and the results are shown in Table S7. It is observed that calculated wt% of total ligand content (L1 + L2) in the mixed linker CPs are closed to their theoretical values obtained from their empirical

formula Ag₂(C₈H₄O₄)_{1-x}(C₈H₅O₄N)_x. Additionally, we have estimated the initial content (wt% or atomic %) of Ag⁰ in Ag@Ag(I)-CP and Ag@Ag(I)-CP (40% NH₂) from their TG curve (Table S7) and the detailed calculation are shown in SI. It has been found that the initial

content of Ag^0 calculated for each structures is ~ 27 at% with respect to total silver or a 17 wt% Ag^0 loading on the $\text{Ag}@\text{Ag(I)-CP}$ materials. These atomic % values are quite higher than the atomic% values (12–14%) obtained from XPS measurements (Table S5), which indicates that the Ag^0 nanoparticles are mostly confined to the bulk of the CP structures.

3.2. Photophysical and photoelectrochemical properties

3.2.1. UV–visible–NIR absorption (DRS) and theoretical (DFT) studies

The optical absorptions of as-prepared samples were measured by UV–vis–NIR DRS. Parent CP showed an absorption band edge at 330 nm in the UV region [15], while a new band appeared at $\lambda_{\text{max}} = 380$ nm with band edges at 427 nm, 432 nm (Fig. 7a) for Ag(I)-CP (20% NH_2), Ag(I)-CP (40% NH_2), respectively. In contrast, to the absorption of L1 and parent CP, a significant shift of absorption into the visible light region occurred after amine incorporation, which is attributed to electron excitation from $-\text{NH}_2$ to the metal state/or π^* of the ligand [17,19,20]. The bandgaps of Ag(I)-CP (0, 20, 40% NH_2) can be calculated using the Kubelka–Munk plot. Fig. 7b shows that the plots of $[F(R)h\nu]^2$ vs $h\nu$ for Ag

(I)-CP (0, 20, 40% NH_2) which are nearly linear at the absorption edge, indicating a direct transition. Extrapolation to the $h\nu$ axis gives band gap estimates of 3.75, 2.90 and 2.87 eV, for Ag(I)-CP , Ag(I)-CP (20% NH_2) and Ag(I)-CP (40% NH_2), respectively [17]. In order to fully understand the importance of L2 for the optical properties of the mixed ligand Ag (I)-CPs, DFT models were constructed in which 50% of L1 was substituted by L2 and a detailed electronic structure of the mixed ligand CP was calculated using a hybrid exchange–correlation functional (HSE06; Fig. 7c and Fig. S12). Fig. 7c shows the calculated band structure of the mixed ligand CP along the high symmetry directions in the first Brillouin Zone (BZ) with the energy referenced to the calculated highest occupied state. Amine functionalization introduces a well separated narrow band at 0 eV due to 2p orbitals of N (lone pair) and C (Fig. S12). The flat nature of this discrete band ensures a direct optical band gap of ~ 2.8 eV at k -points Z and T_2 . This matches well with the onset of optical absorption seen in the experimental UV–vis spectra ($\lambda_{\text{onset}} \sim 430$ nm; $E_g \sim 2.9$ eV, Fig. 7a) for the Ag(I)-CP (20% NH_2), and Ag(I)-CP (40% NH_2). Between -0.8 to -4.4 eV, a dense band structure is observed due to localized and filled 4d states of Ag which mix with the 2p orbitals of O and C of the ligand molecules. In the parent CP we have

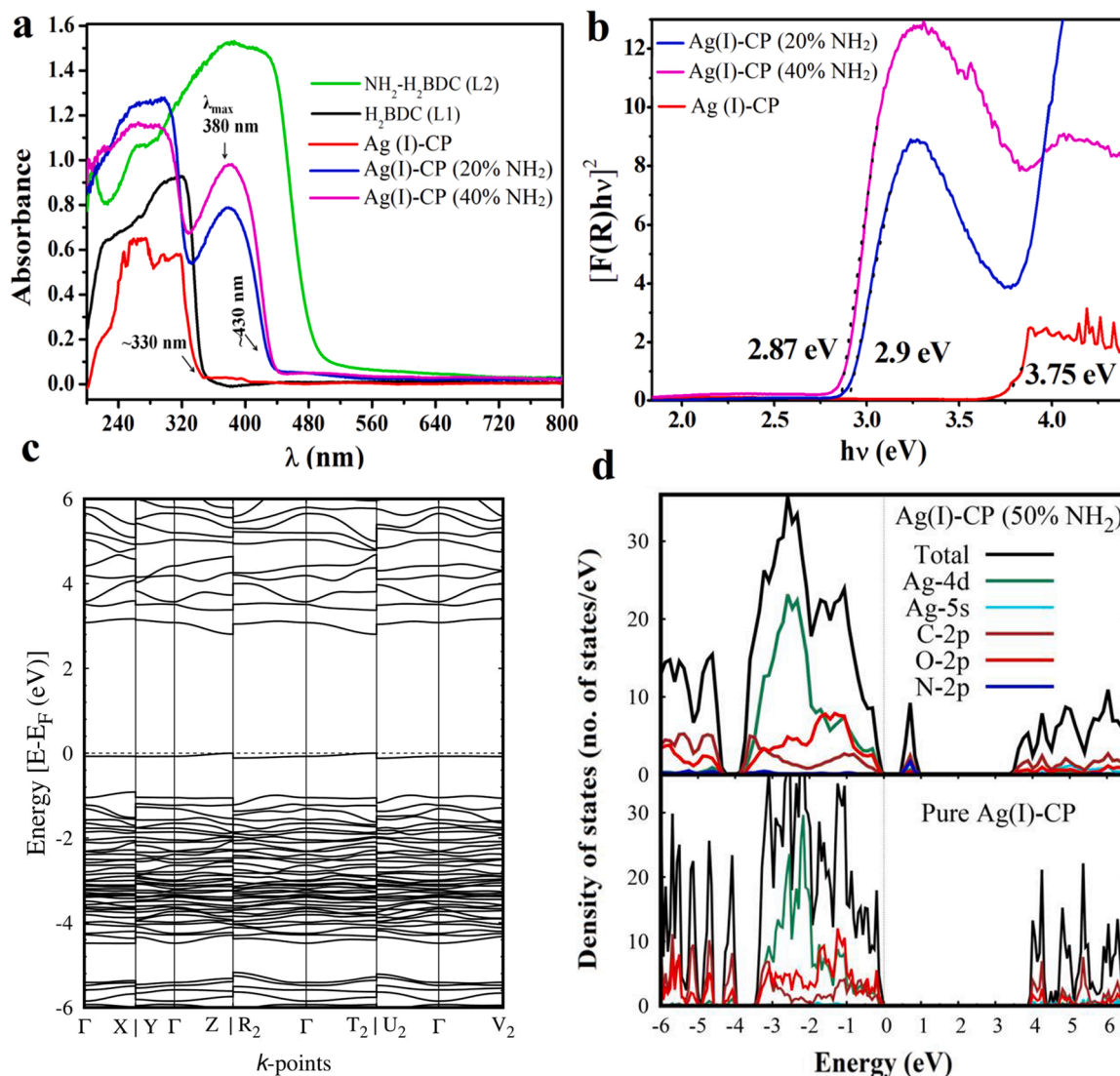


Fig. 7. (a) UV–visible–NIR absorption spectra (solid-state DRS) of the free ligands (L1, L2), parent CP and mixed ligand CPs, and (b) the Kubelka–Munk plot for the corresponding CPs. (c) Band structure of amine functionalized mixed ligand CP (HSE06 hybrid exchange–correlation) (d) Density of States (DOS) and partial-DOS of the mixed ligand CP (top) and parent CP (bottom) [15] as calculated with HSE06 hybrid exchange–correlation. The energy level of the Valence Band Maxima (VBM) is aligned at 0 eV.

previously reported a calculated band gap of 4.0 eV obtained using similar methodology with the corresponding UV–vis optical absorption transition being seen at 330 nm (~ 3.7 eV) [15]. The mixed ligand CP, calculations indicate a similar VBM-CBM separation of 3.7 eV and at the same wavelength (330 nm), a second absorption edge is seen in the experimental UV-Vis measurements for the Ag(I)-CP (20% NH_2), and Ag(I)-CP (40% NH_2) materials. In effect, the amine functionalization has reduced the minimum energy gap of light absorption by the introduction of a localised occupied crystal orbital above the valence band maximum of the system. The density of states (DOS) of mixed ligand CP and parent CP [15] are compared in Fig. 7d with the VBM used to align the energy scales. Amine functionalization of the CP resulted in the formation of a discrete and well separated highest occupied crystal orbital (HOCO), which lies 0.8 eV above the VBM. This localised orbital (state) is composed of an admixture of the non-bonding N-2p orbitals with the 2p orbitals of the aromatic C. There is also some contribution from the Ag-4d and O-2p orbitals. The remaining features of the DOS including the CBM in the mixed ligand CP are similar to the parent CP. Accordingly, the valence band is found between -4.0 and 0 eV (or -4.8 and -0.8 eV for the non-aligned original DOS), where the DOS is composed of mixing between the 4d states of Ag which gives a major contribution to the low energy region with the 2p orbitals of O and C. The lowest unoccupied crystal orbital (LUCO) at the bottom of the conduction band is made up of mostly 2p contributions from aromatic C and O with some small component of Ag-5s. Hence excitations would mostly result from N-2p $\rightarrow \pi^*$ and $\pi \rightarrow \pi^*$ transition with the excitation from the localised N-2p state occurring at lower energies.

Beside the characteristic absorption bands of Ag(I)-CPs, when Ag NPs are introduced *in situ* a localised surface plasmon resonance (LSPR) band was also observed in the Ag@Ag(I)-CP and Ag@Ag(I)-CP(40% NH_2) heterostructures peaking at 432 nm and 480 nm, respectively (Fig. 8a). The absorption edge for the functionalized Ag(I)-CP in Ag@Ag(I)-CP (40% NH_2) is also slightly red shifted, whereas no change of characteristic absorption edge for Ag(I)-CP in Ag@Ag(I)-CP was observed. This result indicates that a stronger interface interaction between the Ag NPs and the coordination polymer is obtained in Ag@Ag(I)-CP(40% NH_2) than in Ag@Ag(I)-CP [51]. In addition, comparing the absorption spectra of these two heterostructures, the LSPR band of the Ag NPs occurs at 432 nm in Ag@Ag(I)-CP whereas the band peak for Ag@Ag(I)-CP

(40% NH_2) is at a longer wavelength (480 nm), which is attributed to a larger size of the Ag NPs in the Ag@Ag(I)-CP(40% NH_2). We also observe that there is a slight quenching of the excitons by electron transfer from Ag(I)-CP(40% NH_2) to Ag NPs (evident from PL studies which will be discussed later) [48,50], whereas, no such effect is observed for Ag@Ag(I)-CP.

To get further insight in the coupled structure, work function (Φ) values of mixed ligand coordination polymer (Ag(I)-CP (50% NH_2)), and pure Ag(I)-CP were separately evaluated through DFT within HSE06 approximation (The details of the methodology and calculation are given in the SI and Fig. S14 and S15). The result shows that the work function values of the Ag(I)-CP (50% NH_2), and Ag(I)-CP are 4.49 and 4.69 eV, respectively. Comparing these values with the work function value of Ag NPs ($\Phi_{\text{Ag}} = 4.7$ eV) [52] in the Fig. 8b, it was found that $\Phi_{\text{Ag(I)-CP}}$ is similar to Φ_{Ag} , while $\Phi_{\text{Ag(I)-CP(50% NH}_2\text{)}}$ is ~ 0.21 eV lower than the Ag metal. Accordingly, the fermi level of Ag(I)-CP (50% NH_2) is above the fermi level of Ag NP. Thus, a Schottky barrier/junction will be formed when Ag NPs couples to the mixed ligand coordination polymer (Ag(I)-CP (50% NH_2)) component.

3.2.2. Photocurrent and EIS measurements

The role of Ag NPs in the Ag@Ag(I)-CP and Ag@Ag(I)-CP (40% NH_2) catalysts in enhancing charge-separation was evaluated by measuring the photocurrent responses for these materials and for Ag(I)-CP and Ag(I)-CP (40% NH_2) (Fig. 9a) under the full spectrum of light from a 300 W Xe lamp. The response was measured for a series of short illumination sequences followed by time without light and the photocurrent was followed over time. As illustrated in our earlier report [15], Ag(I)-CP gives only a small photocurrent response peaking at around 0.1 mA cm^{-2} during the light on part of the experiment and this is also found in the experiment presented in Fig. 9a. Ag(I)-CP has a band gap outside of the visible region (3.7 eV) which originates from LCCT feature and so photogeneration using this solar spectrum simulator source has only low efficiency [15]. Ag(I)-CP (40% NH_2), on the other hand, gives a peak photocurrent of 1.1 mA cm^{-2} so that the lower photon energy for the onset of optical absorption observed from DRS measurements (Fig. 7a) can also lead to charge separation and the production of a larger photocurrent. The *in-situ* deposition of Ag^0 nanoparticles for both ligand systems leads to a significant enhancement of the photogenerated

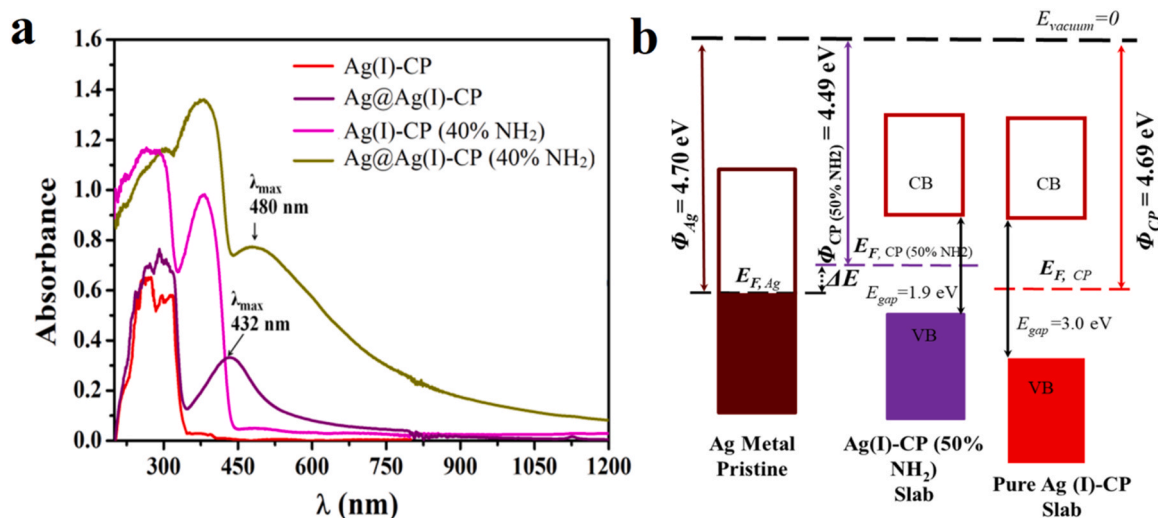


Fig. 8. (a) UV–visible–NIR absorption spectra (solid-state DRS) of the Ag@Ag(I)-CP, and Ag@Ag(I)-CP (40% NH_2) in contrast to their CP counterparts and (b) Schematic diagram of the work function (Φ) calculations which is defined as, $\Phi = E_{\text{vacuum}} - E_{\text{Fermi}}$, where E_{vacuum} and E_{Fermi} are the energy corresponding to the vacuum and Fermi level, respectively: (left) pristine Ag metal obtained from experiments [52], (centre) Ag(I)-CP (50% NH_2) slab with 8 layers, and (right) Ag(I)-CP slab with 4 layers. The valence (VB) and conduction (CB) bands are denoted by boxes. Work functions of the two CPs (centre and right) are calculated within HSE06 approximation. VASP ($E_{\text{Fermi,VASP}}$) calculations place Fermi level on the top of VB. However, to mimic the finite temperature effects in the two semiconductors, the Fermi level (E_F) was shifted to the middle of the band gap (E_{gap}) and this value was used for the work function calculations.

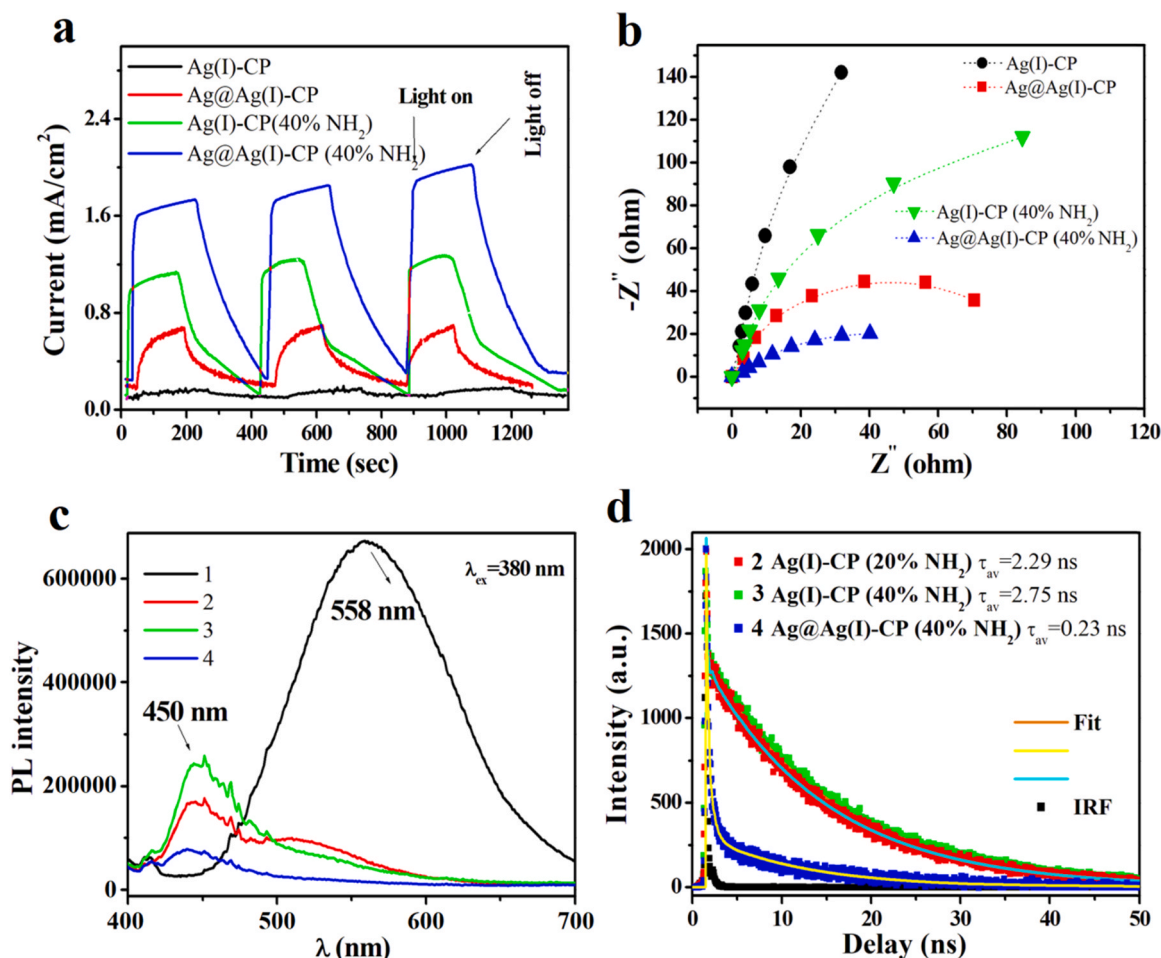


Fig. 9. (a) Photocurrent responses (300 W Xe lamp) for each on-off cycle, and (b) EIS plot of the Ag(I)-CPs (0.5 M *aq.* Na₂SO₄, pH ~ 7). (c) Photoluminescence spectra of (1) free ligand NH₂-bdcH₂ (L2), (2) Ag(I)-CP (20% NH₂), (3) Ag(I)-CP (40% NH₂), (4) Ag@Ag(I)-CP (40% NH₂), upon excitation ($\lambda_{\text{ex}} \sim 380$ nm) and (d) Time-resolved PL spectra and lifetime measurements for Ag(I)-CP (20% NH₂), Ag(I)-CP (40% NH₂), and Ag@Ag(I)-CP (40% NH₂).

current. Ag@Ag(I)-CP has a peak photocurrent around 0.6 mA cm^{-2} and Ag@Ag(I)-CP (40% NH₂) a peak value of 1.7 mA cm^{-2} and a peak shape suggesting that the photocurrent was increasing at the end of the light on section of the experiment. Additionally, it was also observed from the Nyquist plot (Fig. 9b) and Mott Schottky plot (Fig. S15) that among the Ag(I)-CPs, Ag@Ag(I)-CP (40% NH₂) exhibited lowest charge transfer resistance and highest charge carrier density. These results show that not only can the Ag NPs improve absorption of light in the visible region due to their LSPR absorptions [53,54], but that carrier separation is also more efficient for materials with Ag NPs present.

3.2.3. PL studies

Solid-state PL measurements were also carried out for the catalyst samples with the resulting spectra shown in Fig. 9c. The free ligand, L2 (2-amino 1, 4 benzene dicarboxylic acid) shows a radiative emission at 558 nm upon excitation by light with $\lambda_{\text{ex}} = 380$ nm consistent with its ligand centred transition features [44]. The characteristic radiative emission of L2 in mixed linker CPs (Ag (I)-CP (20% NH₂) and Ag (I)-CP (40% NH₂)) is observed at 450 nm with a hypsochromic shift of ~ 110 nm due to loss of co-planarity of the L2 ligand upon bonding with Ag⁺ [17]. Besides blue shifting, the intensity of the emission for both the mixed linker CP is decreased in compared to the free ligand (L2). Note that emission at 450 nm for the mixed linker CPs is occurred upon excitation at the wavelength 380 nm. This excitation wavelength corresponds to the characteristic absorption maxima of the mixed linker CPs and occurred only for the presence L2 ligand as observed in the

UV-vis-NIR study (Fig. 7a). Thus, free L2 at its highest content (100%) absorbs maximum light at this excitation wavelength and excited to the higher energy level. As the L2 content decreased to 40%, PL intensity of the Ag (I)-CP (40% NH₂) is decreased. Likewise a lowest PL intensity has been observed for the Ag (I)-CP (20% NH₂). However, a different result was obtained for the Ag@Ag(I)-CP (40% NH₂) material, which shows a much lower intensity emission with the peak shifted to a shorter wavelength (~ 440 nm). Clearly this suggests that Ag NPs act to increase the lifetime of photogenerated charge carriers [55,56]. Meanwhile, the time-resolved PL spectra of the samples are shown in Fig. 9d and their lifetime decay fitting parameters are listed in Table S8. It shows the average lifetimes of Ag(I)-CP (20, 40% NH₂) are at around 2.29–2.75 ns. Notably, the lifetime of Ag@Ag(I)-CP (40% NH₂) was reduced to 0.23 ns, indicating the deposition of Ag NPs facilitates the transfer of charge carrier and speed up the charge transfer between the Ag(I)-CP (40% NH₂) and Ag NPs [57]. Hence, we conclude that Ag NPs not only show LSPR effects but also form a Schottky junction with the coordination polymer component of these catalysts.

3.3. Photocatalytic oxidation of benzyl alcohol

3.3.1. Performance of the prepared materials

The photocatalytic activities of the as-prepared samples were tested for the oxidation of benzyl alcohol (BA) under visible light irradiation ($\lambda \geq 420$ nm) in the presence of oxidant (O₂, H₂O₂ and K₂S₂O₈) at ambient temperature. To identify the reactants and products in the

reaction mixture, the retention times of their standard samples are first measured from the HPLC (Fig. S16–S18) and then the progress of the reactions were studied. Fig. S19 and S20 gives example HPLC measurements for a reaction using the Ag@Ag(I)-CP (40% NH₂) photocatalyst. During light irradiation the measured concentration of BA decreases with time, while a new peak appears which was identified as benzaldehyde (BD) from the GC-MS (Gas chromatogram: Fig. S21, Mass spectra: Fig. S22 and 23). Catalytic data from experiments using the range of materials synthesised for the project and comparing oxidants are summarised in Table 3. The conversion of BA to BD in presence of Ag(I)-CP was very low when using our standard conditions with O₂ as oxidant (Table 3, entry 1): 6 h of light irradiation from the Hg lamp source ($\lambda \geq 420$ nm). This was as expected since the parent CP material has too large a band gap (3.75 eV) to be activated under visible light conditions. Conversion (13%) is observed when the corresponding catalyst containing Ag⁰ nanoparticles, Ag@Ag(I)-CP is used as a catalyst with O₂ under the same conditions (Table 3, entry 2), indicating that the LSPR band of the Ag-NP component of the material is able to take part in photo-generation of oxidising species. A similar conversion is seen from the photocatalytic experiments using mixed ligand Ag(I)-CP materials even without the introduction of Ag NPs (Table 3, entry 3) and the conversion increases further to 16% at the higher loading of L2 (Table 3, entry 4). Again, this implies that the decrease in the optical absorption band gap on the introduction of the amine substituent on the linker molecule (Fig. 7) is sufficient to allow photocatalysis to take place. The highest BA conversion (22%) and BD yield (19%) obtained using O₂ as oxidant were achieved with Ag@Ag(I)-CP (40% NH₂) as the photocatalyst (Table 3, entry 5). The activity of the Ag@Ag(I)-CP (40% NH₂) and Ag(I)-CP (40% NH₂) catalyst also tested under the same experimental condition using 30% (w/v) of H₂O₂ as an external and green oxidant. The result clearly tells that conversion of BA is increased in compare to that of oxidant O₂ (Table 3, entry 6–7). Among these two catalyst, the highest BA conversion (42%) and BD (yield 29%) obtained using H₂O₂ were achieved with Ag@Ag(I)-CP (40% NH₂). This again ascertains the crucial role of Ag NPs in the structure. Notably, the selectivity of BD for both the catalyst (69–75%) was greatly reduced in presence of H₂O₂. Addition of H₂O₂ though increases the rate of BA oxidation however it reduced the selectivity for both the catalysts. In general H₂O₂ dissociates under the action of photogenerated electron or the protic solvent water present in the H₂O₂ under the action of

photogenerated hole may split into •OH radical [58]. This •OH radical is highly nonselective and may cause the over oxidation of BD. For experiments using K₂S₂O₈ as oxidant the reaction time was decreased to 4 h as the reaction rate was found to be higher than that with O₂ and H₂O₂. Conversion and yield data are consistently higher with K₂S₂O₈ and even the parent CP material gives 10% conversion with this oxidant (Table 3, entry 8). Again, activity increases when either Ag NPs or amine substituted ligands are introduced into the Ag(I)-CP catalysts (Table 3, entries 9 and 10). For the mixed ligand material Ag(I)-CP (40% NH₂) a conversion of 46% and a BD yield of 42% is obtained (Table 3, entry 11), which is enhanced upon usage of the corresponding heterostructured catalyst Ag@Ag(I)-CP(40% NH₂). In addition, the selectivity to BD is consistently over 90% for the K₂S₂O₈ oxidant, suggesting that over-oxidation is limited. The higher oxidation rates using K₂S₂O₈ can be understood in terms of the higher electron affinity of this oxidant compared to gaseous phase O₂ and the fact that its use does not involve a liquid/gas interface to deliver the oxidising species [59]. In the absence of light and catalyst, no reaction takes place (Table 3, entry 13) and without catalyst there is no significant photochemistry (Table 3, entry 14). Even with our most active catalyst the reaction without illumination proceeds only slowly so that only a 14% conversion is seen after 4 h for the reaction using Ag@Ag(I)-CP (40% NH₂) in the dark with the K₂S₂O₈ oxidant (Table 3, entry 15) compared with 57% conversion for the same system with visible light (Table 3, entry 12). These results demonstrate that catalytic performance is promoted under the light irradiation and that the major part of the oxidation chemistry observed is photocatalytically driven. For reliable understanding of the merits of the mixed ligand CP and Ag NPs coupled mixed ligand CP, a comparison of their activities (in presence K₂S₂O₈) on BA oxidation reaction has been made with synthesized Ce-UIO-66 (NH₂), Ag@Ce-UIO-66 (NH₂), Ag@TiO₂, and Ag@ZnO samples (See details in SI and Fig. S24). The results shown in Table 3, entry 16–17, clearly indicate Ag@TiO₂, and Ag@ZnO is able to catalyse only the 10%, and 12% of BA with yield of 9% and 8% of BD, respectively. The oxidation is here mainly initiated by the SPR effects of Ag NPs [50,51]. Mixed ligand MOF like Ce-UIO-66 (NH₂) and its Ag NPs coupled structure Ag@Ce-UIO-66 (NH₂) are able to catalyse 31% and 39% of BA with yield 27.6% and 30.0% of BD, respectively (Table 3, entry 18–19). The above results indicates both the components such as Ag NPs and amine functionalization individually do function for BA oxidation, however they play best when a coupled

Table 3
Photocatalytic oxidation of benzyl alcohol to benzaldehyde over prepared catalysts.

Entry	Catalyst	Solvent	Oxidant	Conversion/%	Selectivity/%	Yield/%
1	Ag(I)-CP	CH ₃ CN	O ₂ ^a	trace	–	–
2	Ag@Ag(I)-CP	CH ₃ CN	O ₂ ^a	13	80	10.4
3	Ag(I)-CP (20% NH ₂)	CH ₃ CN	O ₂ ^a	12	84	10.1
4	Ag(I)-CP (40% NH ₂)	CH ₃ CN	O ₂ ^a	16	90	14.4
5	Ag@Ag(I)-CP (40% NH ₂)	CH ₃ CN	O ₂ ^a	22	87	19.1
6	Ag(I)-CP (40% NH ₂)	CH ₃ CN	H ₂ O ₂ ^a	35	75	26.2
7	Ag@Ag(I)-CP (40% NH ₂)	CH ₃ CN	H ₂ O ₂ ^a	42	69	29.0
8	Ag(I)-CP	CH ₃ CN	K ₂ S ₂ O ₈ ^b	10	97	9.7
9	Ag@Ag(I)-CP	CH ₃ CN	K ₂ S ₂ O ₈ ^b	31	94	29.1
10	Ag(I)-CP (20% NH ₂)	CH ₃ CN	K ₂ S ₂ O ₈ ^b	26	96	24.9
11	Ag(I)-CP (40% NH ₂)	CH ₃ CN	K ₂ S ₂ O ₈ ^b	46	92	42.3
12	Ag@Ag(I)-CP (40% NH ₂)	CH ₃ CN	K ₂ S ₂ O ₈ ^b	57	95	54.1
13	–	CH ₃ CN	K ₂ S ₂ O ₈ ^c	trace	–	–
14	–	CH ₃ CN	K ₂ S ₂ O ₈ ^b	trace	–	–
15	Ag@Ag(I)-CP (40% NH ₂)	CH ₃ CN	K ₂ S ₂ O ₈ ^c	14	97	13.6
16	Ag@TiO ₂	CH ₃ CN	K ₂ S ₂ O ₈ ^b	10	98	9.8
17	Ag@ZnO	CH ₃ CN	K ₂ S ₂ O ₈ ^b	12	96	9.6
18	Ce-UIO-66 (NH ₂)	CH ₃ CN	K ₂ S ₂ O ₈ ^b	31	89	27.6
19	Ag@Ce-UIO 66 (NH ₂)	CH ₃ CN	K ₂ S ₂ O ₈ ^b	39	95	37.0

Reaction conditions, photocatalyst 25 mg (0.065 mmol and 32.5 mol%), 0.2 mmol of benzyl alcohol, 50 mL solvent, light source: 250 W Hg lamp ($\lambda \geq 420$ nm), light intensity = 3.7 mW cm⁻², oxidant O₂, 0.3 mmol of H₂O₂ (30%: w/v), 0.22 mmol of K₂S₂O₈ as indicated. Product identification by GC and HPLC, yield from HPLC.

^a 6 h light irradiation.

^b 4 h light irradiation.

^c 4 h in dark.

structure is formed with Ag^+/Ag^0 based system.

Table S9 shows apparent quantum efficiency (AQE) values for BA oxidation (the details of the calculation are shown in SI) in the presence of various Ag(I)-CP solids; Ag(I)-CP (40% NH_2) achieved AQE values of 1.08% and 4.78% and Ag@Ag(I)-CP (40% NH_2) gave AQE values of 1.44% and 6.12% each in presence of O_2 and $\text{K}_2\text{S}_2\text{O}_8$, respectively. Indeed, Ag@Ag(I)-CP (40% NH_2) demonstrated superior photocatalytic activity to all other materials tested in terms of conversion, yield and AQE under our standard conditions. A comparison of catalytic performance including AQE values for the oxidation of BA to BD for Ag@Ag(I)-CP (40% NH_2) with example photocatalysts for this reaction reported in the literature is made in Table 4 [60–67]. Tanaka et al. [60] have used a photoreductive deposition method to produce Au NP catalysts supported on CeO_2 (Table 4, entry 1). The semiconducting ceria support material is used as the photo-reducing agent for the HAuCl_4 salt solution. They find that the most active catalysts are produced by preparing the catalyst in a series of reduction processes so that the desired loading is built up in stages. Pt NPs supported on the anatase polymorph of TiO_2 have also been tested for the oxidation of BA to BD (Table 4, entry 2). This system has a low Schottky barrier for the injection of photoelectrons generated on the metal nanoparticles into the semiconducting Titania leading to good charge separation and resulting in a very active oxidation catalyst [61]. Au/ TiO_2 catalysts have also been synthesised from a colloidal Au precursor by Tanaka et al. [62] who found that the well-defined particle size of the resulting catalyst could be controlled by the post-deposition calcination temperature. This allowed the surface plasmon resonance to be tuned between 600 nm and 700 nm. The corresponding change in photocatalysis demonstrated that the plasmon resonance and photocatalytic activity are linked. These precious metal photocatalysts

supported on semi-conducting oxides give impressive performance for the oxidation of BA to BD and the use of NPs allows good AQE values around 7 (Table 4, entries 2 and 3) to be achieved. However, the use of Pt and Au implies a high cost and the use of metals with relatively low earth abundance would make the widespread use of these catalysts challenging. More complex heterostructured oxides have also been used for the photooxidation of BA to BD. Li et al. [63] have synthesised ZnO@TiO_2 heterostructured oxides with a TiO_2 core and ZnO shell, following reports that ZnO could improve the photocatalytic properties of TiO_2 . They show that performance can be improved further by the introduction of metal NPs at the interface between the core and shell oxides and propose that these NPs improve transfer of photogenerated electrons and holes between the semi-conducting oxides. In this case, Au NPs in ZnO@Au@TiO_2 give higher conversion of BA after 1 h of reaction using a Xe lamp as a light source than does the Pt NP containing catalyst ZnO@Pt@TiO_2 (Table 4, compare entries 4 and 5).

However, Ag NPs give the best performance of any catalyst tested in the study with ZnO@Ag@TiO_2 giving an 86% conversion of BA with a 44% BD yield (Table 4, entry 6). However, in these materials the metal NPs are at the interface between the oxides and photo-generated electron-hole pairs are mostly generated in the ZnO outer layer rather than from the plasmon resonance of the nanoparticles. To test the photocatalytic properties of Ag^0 nanoparticles themselves Chen et al. [64] used wide bandgap oxide supports so that reaction data could be ascribed to the nanoparticles alone. These catalysts showed some BA conversion demonstrating that Ag^0 nanoparticle plasmon excitations can generate oxidising species from O_2 (Table 4, entry 7). Other metals have also been supported on wide bandgap porous materials with Cu (Table 4, entry 8) and Pd (Table 4, entry 9) showing much higher

Table 4

A survey of performance of noble metal supported photocatalysts for the oxidation benzyl alcohol (BA) to benzaldehyde (BD).

Entry	Photo catalysts	Solvent and oxidant	Light λ /nm P ^a /mW cm ⁻² time, t/h	Conv. BA/%	Yield BD/%	AQE ^a /% (λ /nm)
1	1% ^b Au/ CeO_2 [60]	Water, O_2	Green LED, $\lambda_c^c = 530$ P = 1.7 t = 24	59	59	3.1 (530)
2	2% ^b Pt/ TiO_2 [61]	Toluene, O_2	$300 < \lambda < 800$ P = 8.1 t = 4	75	72	7.0 (550)
3	1% ^b Au/ TiO_2 [62]	Water, O_2	$600 < \lambda < 700$ P = 1.7 t = 12	> 99	> 98	7.2 (625)
4	TiO_2 @Pt@ZnO [63]	Water, Air	300 W Xe ^d t = 1	45	24	–
5	TiO_2 @Au@ZnO [63]	Water, Air	300 W Xe ^d t = 1	83	36	–
6	TiO_2 @Ag@ZnO [63]	Water, Air	300 W Xe ^d t = 1	86	44	–
7	Ag/zeolite Y [64]	Toluene, O_2	$\lambda > 365$ P = 14 t = 48	11	7	–
8	0.1%Cu@UiO-66(Zr) [65]	CH_3CN , O_2	$\lambda \geq 400$ t = 3	50	50	–
9	Pd/MIL-125- NH_2 [66]	CH_3CN , Air	$360 < \lambda < 780$ P = 100 t = 8	36	36	–
10	MIL-125/Ag/g- C_3N_4 [67]	CH_3OH , O_2	$\lambda > 400$ t = 6	65	64	–
11	Ag@Ag(I)-CP (40% NH_2) (This work)	CH_3CN , O_2	$\lambda > 420$ P = 3.7 ^f t = 6	22	19	1.4 (436)
12	Ag@Ag(I)-CP (40% NH_2) (This work)	CH_3CN , $\text{K}_2\text{S}_2\text{O}_8^c$	$\lambda > 420$ P = 3.7 ^f t = 4	57	54	6.1 (436)

^a Power.

^b weight % loading of metal.

^c reported wavelength of maximum intensity for green LED light source.

^d A 300 W Xenon short arc lamp used as solar simulation source.

^e 0.22 mmol of oxidant used in reaction.

^f The intensity of the light in this work was obtained by using potassium ferrioxalate Actinometry experiments (the detailed experiment is presented in the SI).

conversions [65,66]. Coupling Ag^0 nanoparticles with the narrow band gap material graphitic carbon nitride ($\text{g-C}_3\text{N}_4$, $E_g = 2.45$ eV) was also found to greatly improve activity [67]. The best performance of the new materials presented here was found for the Ag nanoparticles coupled with the narrow band gap Ag(I)CP (40% NH_2), i.e.: Ag@Ag(I)CP (40% NH_2). This material, particularly when used with an inorganic oxidant, has a comparable performance with previous materials for the BA oxidation in terms of conversion, yield and AQE values, including those materials reliant on precious metals.

3.3.2. Stability in reuse tests

A reuse test of the Ag(I)-CP (40% NH_2) and Ag@Ag(I)-CP (40% NH_2) catalysts for the BA oxidation to BD using $\text{K}_2\text{S}_2\text{O}_8$ as oxidant was also carried out as part of this work. Fig. 10a shows that over the series of seven reuse tests the Ag(I)-CP (40% NH_2) loses activity significantly, with the first run BA conversion of 46% being reduced by a factor of 2.7 to only 17% for the 7th cycle. Whereas, Ag@Ag(I)-CP (40% NH_2) retains its performance with BA conversion only falling from 57% to 41% over the seven experiments.

Initially, the phase and structural integrity of the photocatalyst in the middle of this reaction sequence (after 4th cycle) were analysed by PXRD (Fig. S25a) and XPS (Fig. S25b). The PXRD pattern for Ag@Ag(I)-CP (40% NH_2), shows a new peak corresponding to Ag^0 after the reuse sequence of experiments, which indicates that partial reduction of lattice Ag^+ has taken place during photocatalysis. High resolution XPS spectra (Fig. 10b) in the region of the Ag 3d peak can be de-convoluted to measure the atomic% of Ag^0 (Table S10) present in the catalyst samples. This revealed that the atomic% of Ag^0 in Ag(I)-CP (40% NH_2)

and Ag@Ag(I)-CP (40% NH_2) after the 4th cycle were 18.9% and 18.1%, respectively. This means that the amount of Ag^0 present in Ag@Ag(I)-CP (40% NH_2) is increased by a factor of around 1.3 from its initial content (14.7%) and it has been estimated that only 4% of Ag(I) has been reduced. On the other hand, the amount of Ag^0 present in Ag(I)-CP (40% NH_2) has increased by a factor of around 5.5 corresponding to 16% of lattice Ag(I) being reduced and migrating to form the Ag^0 particles seen by PXRD over the course of the reuse cycles. Beside the phase analysis and estimation of surface composition, local structure of both the photocatalysts and compositions of the L2 content in each structure were investigated after photocatalytic experiments (7th cycle). For such investigation each sample after use was washed with water and ethanol, dried, and followed the alkaline lysis route. Fig. S26 depicts the ^1H NMR spectra of the solid obtained after the neutralization of the digested solution of the fresh and used photocatalysts. It shows that both the L2 proton signals ($3 \times ^1\text{H}$: H2, H3, H4) and L1 proton signal ($4 \times ^1\text{H}$: H1) remains unaltered (Fig. 10c). No additional signals were observed after the photocatalytic reaction, which indicates that both the ligand remains intact with their respective functional groups and aromatic moiety in the Ag(I)-CP (40% NH_2) and Ag@Ag(I)-CP (40% NH_2) samples. However, unlike the positions of signals for each structure, the intensity of the L2 signal with respect to L1 was found to alter in each sample after the photocatalytic treatment. To verify such observation a quantitative estimation of the L2 in the used photocatalysts was carried out from the UV-visible spectroscopic study of the digested samples (Fig. S27a). It shows that Ag(I)-CP (40% NH_2) and Ag@Ag(I)-CP (40% NH_2) loses the L2 content (mol%) after the photocatalytic experiment by a factor of 2.8, and 1.3, respectively (Table S6 and Table S11). Furthermore total ligand

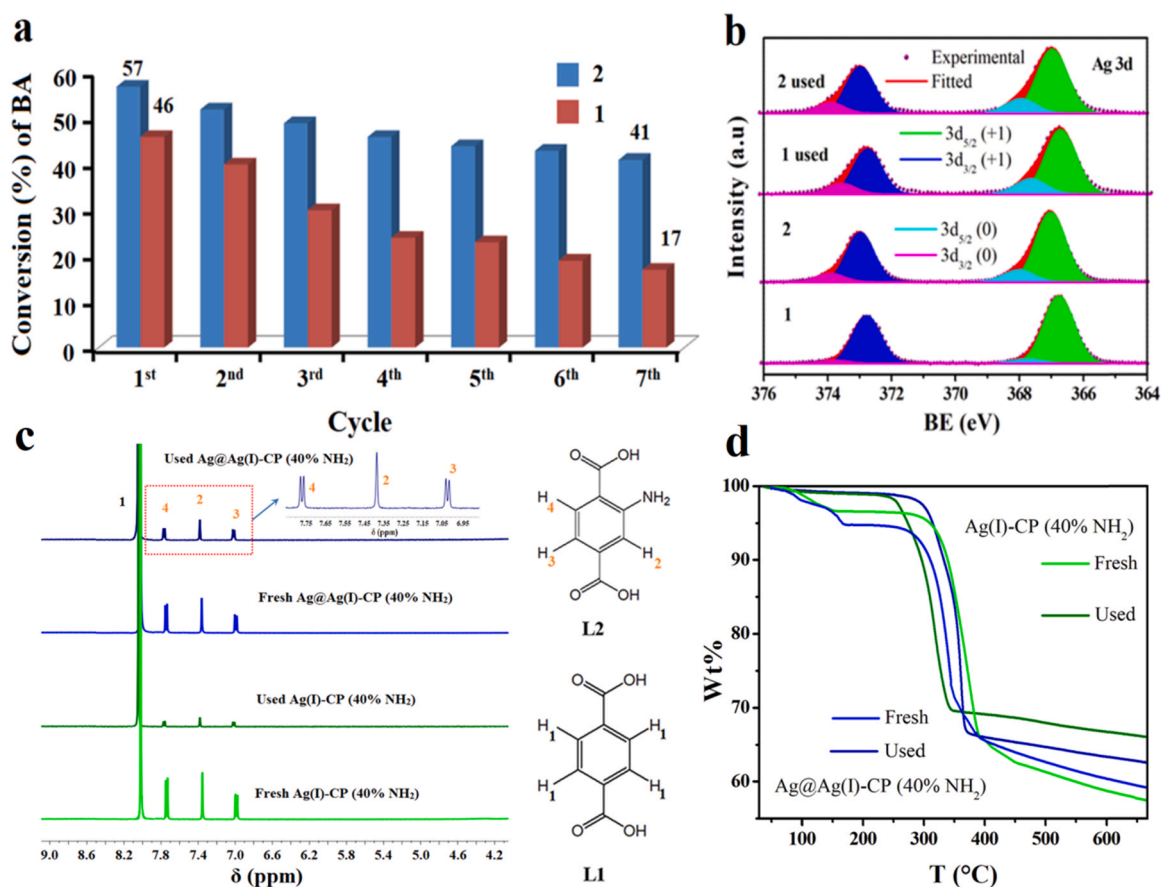


Fig. 10. (a) Recyclability test of the (1) Ag(I)-CP (40% NH_2), and (2) Ag@Ag(I)-CP (40% NH_2) for the photocatalytic oxidation of BA under visible light irradiation up to 7th cycle, and (b) high resolution Ag 3d XPS images of the photocatalysts before and after used for 4th cycle. (c) Normalized ^1H NMR spectra of the solid obtained after neutralization by 0.2 M HCl from the digested CPs (fresh and used after 7th cycle) in DMSO (d_6): proton signal (1) associated with L1 and (2–4) signals associated with L2. (d) TGA profile of fresh and used Ag(I)-CP (40% NH_2), and Ag@Ag(I)-CP (40% NH_2) in N_2 atmosphere.

content (L1 + L2) was estimated from the TG analysis of the used photocatalysts and compared with that of the fresh samples (Fig. 10d). The result shows that wt. (%) loss in the mixed like CP corresponds to the total ligand (L1 + L2) has significantly reduced (45.4–32.9%) when it is used in the photocatalytic reaction. Whereas no such major reduction of total ligand content was observed for Ag NPs coupled mixed linker CP (Table S7, Table S11). The above result underscores that ligand (mostly L2) dissolute from the mixed linker CP when it is uncoupled during the photocatalytic reaction, whereas no such significant loss of L1 and L2 was observed from the Ag NPs coupled mixed linker CP. Such high stability of the coupled structure has also been observed from its HRTEM study (Fig. S27b) and realized by calculating Ag NPs (Ag^0) content from its TG curve (Fig. 10d). The Ag^0 content in used $\text{Ag}@\text{Ag}(\text{I})\text{-CP}$ (40% NH_2) is calculated to be 29.3 at% which is slightly increased from its initial value (27.6 at%) whereas for the same period of photocatalytic cycle the Ag^0 content in the $\text{Ag}(\text{I})\text{-CP}$ (40% NH_2) was found to be 55.4 at% (Table S7 and Table S11). Thus the loss of the ligand can be understood correlating with the reduction of Ag^+ . In terms of the electron accepting properties of the lattice Ag^+ cations, the reduction of it in the uncoupled mixed linker CP is much higher than that of the reduction of the oxidant ($\text{O}_2/\text{K}_2\text{S}_2\text{O}_8$) during photocatalysis. Whereas, in the case of $\text{Ag}@\text{Ag}(\text{I})\text{-CP}$ (40% NH_2), Ag^0 already present in the structure can promote the multi-electron transfer process by pooling and transferring photogenerated electrons to the oxidant $\text{K}_2\text{S}_2\text{O}_8$ (or O_2) [28], thereby maintaining the Ag^+/Ag^0 ratio in the structure and stabilising the photocatalyst against dissolution of the ligand in mixed ligand CP structure.

3.3.3. Kinetics of BA oxidation

The reaction kinetics of the BA to BD conversions using prepared catalysts was studied as shown in Fig. S28 and their kinetic parameters are listed in Table S12. For either oxidant the lowest rate constant value was obtained with the $\text{Ag}(\text{I})\text{-CP}$ catalyst and the rate constant value are then enhanced for $\text{Ag}(\text{I})\text{-CP}$ (20% NH_2) and $\text{Ag}(\text{I})\text{-CP}$ (40% NH_2), and achieved highest values with $\text{Ag}@\text{Ag}(\text{I})\text{-CP}$ (40% NH_2). The result shows that the lowering of the optical absorption threshold and enhancement of porosity by amine functionalisation may leads to more effective photooxidation catalysts. However, note that the surface area of the coupled structures have been reduced after Ag NP incorporation, thus their enhanced reaction rate could be correlated only if the reaction rate constants are normalized with respect to surface area [68]. The results listed Table S12 show that the intrinsic reaction rate of $\text{Ag}@\text{Ag}(\text{I})\text{-CP}$ (40% NH_2) is $51.0 \times 10^{-6} \text{ min}^{-1} \text{ g}^{-1} \text{ m}^2$ with the O_2 oxidant and $26.7 \times 10^{-5} \text{ min}^{-1} \text{ g}^{-1} \text{ m}^2$ with $\text{K}_2\text{S}_2\text{O}_8$. These values are between 3.6 and 3.7 times that of $\text{Ag}(\text{I})\text{-CP}$ (40% NH_2) without Ag-NPs, ($k = 13.5 \times 10^{-6} \text{ min}^{-1} \text{ g}^{-1} \text{ m}^2$ (O_2) and $k = 7.5 \times 10^{-5} \text{ min}^{-1} \text{ g}^{-1} \text{ m}^2$ ($\text{K}_2\text{S}_2\text{O}_8$)), which implies that photocatalytic activity of $\text{Ag}@\text{Ag}(\text{I})\text{-CP}$ (40%- NH_2) is enhanced presumably due to the ability of the surface plasmon band absorption to generate electrons and holes that can initiate oxidation. Hence, incorporation of amine functionalised linker molecules in the CP and coupling of Ag NPs both are crucial in enhancing photocatalytic activity of the coupled structure.

The species responsible for the oxidation of benzyl alcohol during the photocatalytic reactions in presence of $\text{Ag}@\text{Ag}(\text{I})\text{-CP}$ (40% NH_2) under an O_2 atmosphere was tested by adding nitrobenzene (NB) as an $\bullet\text{OH}$

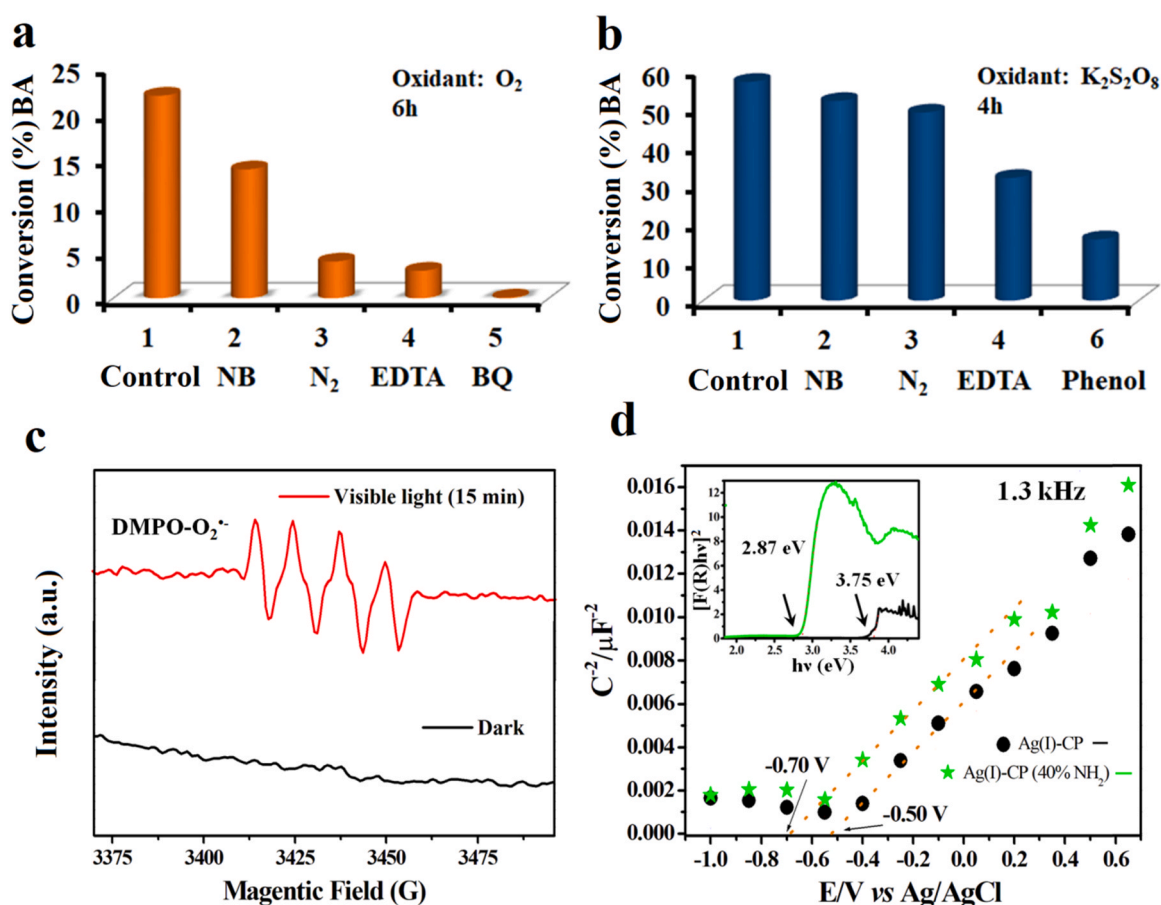


Fig. 11. (a) Conversion of benzyl alcohol using $\text{Ag}@\text{Ag}(\text{I})\text{-CP}$ (40% NH_2) as catalyst under the irradiation of visible light (250 W Hg lamp), with O_2 as oxidant in the presence of scavengers (1) No scavenger (control) (2) NB: nitrobenzene ($\bullet\text{OH}$ scavenger, 10^{-3} M) (3) N_2 atmosphere, (4) EDTA: Na_2EDTA (h^+ scavenger; 10^{-3} M) and (5) BQ: Benzoquinone ($\text{O}_2^{\bullet-}$ scavengers; 10^{-3} M), (b) as (a) using $\text{K}_2\text{S}_2\text{O}_8$ (0.22 mmol) as oxidant and with (6) Phenol ($\text{SO}_4^{\bullet-}$ scavengers; 10^{-3} M). (c) EPR spectra of the $\text{DMPO-O}_2^{\bullet-}$ (O_2 saturated) adduct obtained for the CH_3CN solution containing 20 mM DMPO at 303 K in presence of $\text{Ag}@\text{Ag}(\text{I})\text{-CP}$ (40% NH_2) system before and after visible light irradiation. (d) Mott-Schottky plots for $\text{Ag}(\text{I})\text{-CP}$ and $\text{Ag}@\text{Ag}(\text{I})\text{-CP}$ (40% NH_2) at a frequency of 1300 Hz in 0.5 M $\text{Na}_2\text{SO}_4(\text{aq.})$ solution (pH ~ 7).

scavenger, Na₂EDTA as a hole (h⁺) scavenger and benzoquinone (BQ) as an O₂^{•−} scavenger, (Fig. 11a) [15,49,69]. The time evolution of these reactions is also shown in Fig. S29a and this data were fitted to the pseudo-first order rate expression to obtain apparent rate constant values (Table S13). As shown in Fig. 11a the conversion of BA was strongly affected by reactions carried out with the addition of Na₂EDTA (Conv. 5%, $k = 1.1 \times 10^{-4} \text{ min}^{-1}$) and was completely stopped by the addition of BQ, whereas nitrobenzene was much less effective at inhibiting the oxidation process (Conv. 15%, $k = 4.5 \times 10^{-4} \text{ min}^{-1}$). This infers that the hole (h⁺) produced from photoexcitation is directly involved in the reaction whereas the photoelectron reacts with the oxidant to produce superoxide (O₂^{•−}). In order to confirm the role of O₂ as oxidant, a reaction was also carried out in an N₂ atmosphere which showed a similar drop in conversion to that for Na₂EDTA addition, presumably due to residual oxygen remaining dissolved in solution after the reactor head space atmosphere was switched to N₂. When K₂S₂O₈ is used as an oxidant, the rate of BA oxidation is increased by five-fold for the Ag@Ag(I)-CP (40% NH₂) catalyst. To understand the role of active species with this electron acceptor, we conducted the same series of control experiments by adding the same set of scavengers as used for O₂ reactions. In this case phenol is also added to the scavenger set, phenol and nitrobenzene are both well-known trapping agents for •OH and SO₄^{2•−} species, but phenol provides better specificity for SO₄^{2•−} [69,70]. BA conversion for this set of reactions is given in Fig. 11b and the time evolution data is shown in Fig. S29b, from which rate constants have been derived with values listed in Table S13. Here, again, NB has only a weak influence on the photocatalytic efficiency ($k = 34.7 \times 10^{-4} \text{ min}^{-1}$) while EDTA (h⁺ scavenger) drops the conversion compared to the control experiment by around half with a corresponding reduction in the effective rate constant ($k = 16.9 \times 10^{-4} \text{ min}^{-1}$ cf $k = 38.7 \times 10^{-4} \text{ min}^{-1}$ (control)), (Table S13). On the addition of phenol to the reaction the conversion is reduced significantly and the effective rate constant ($k = 7.5 \times 10^{-4} \text{ min}^{-1}$) is five times lower than seen in the control experiment. These results are consistent with the predominant role of the SO₄^{2•−} radical, which is formed as the main active species on transfer of the photo excited electron to the persulfate anion. This is further confirmed when the reaction is carried out under an N₂ atmosphere which has only a small effect on the observed conversion.

3.3.4. Active species trapping experiments

The formation of superoxide (O₂^{•−}) when O₂ is used as oxidant was also evident from an NBT test [71,72]. Details of the experiment are given in SI and the results are shown in Figs. S30 and S31. A comparative study (Fig. S31b) estimating of the concentration of O₂^{•−} from the reaction stoichiometry given in Scheme S2 and comparisons of the results (O₂^{•−} concentration vs time: Fig. S31b) obtained for each photocatalyst revealed that within 1.5 h of light irradiation the Ag@Ag(I)-CP (40% NH₂) gave the highest efficiency of superoxide production (~95 μM) compared to Ag(I)-CP (40% NH₂) and Ag@Ag(I)-CP. A negligible level of superoxide production was observed with Ag(I)-CP, due to its low photocarrier production rate under visible light illumination. Even so, O₂^{•−} production is observed over Ag@Ag(I)-CP from the active LSPR excitation of the Ag⁰ NPs and promotion of the adsorption of O₂ to the surface [51]. Besides, electron paramagnetic resonance (EPR) analysis was also used using 5,5-dimethyl-1-pyrroline N-oxide (DMPO) to trap and identify the intermediate oxygen species formed during BA oxidation reaction in presence of Ag@Ag(I)-CP (40% NH₂) [73]. The results are depicted in Fig. 11c. Note that no EPR signal can be observed in dark. On the contrary, upon visible light irradiation ($\lambda \geq 420 \text{ nm}$) for 15 min, EPR signal of DMPO-O₂^{•−} adduct is visible, indicating the ability of the catalyst to produce O₂^{•−} from the reduction of O₂. All these facts are in good agreement with the activity results, indicating that the oxidation reaction of benzyl alcohol is facilitated in the photogenerated hole only when the oxidant such O₂ or K₂S₂O₈ get efficiently reduced by the photogenerated electron.

3.4. Photocatalytic mechanism

The Mott–Schottky plot for Ag(I)-CP (40% NH₂) is compared with that for parent CP in Fig. 11d this allows comparison of band-edge potentials and further insight into the nature of their semiconductivity [15,74]. The positive slope obtained from the measurement (C^{−2} vs V Ag/AgCl) indicates that, both parent CP and mixed ligands CP are n-type semiconductors. A small negative shift of the flat band potential was observed for the mixed ligand CP compared to the parent CP material. The calculated flat band potential is found to be −0.70 V vs Ag/AgCl for Ag(I)-CP (40% NH₂). This means that the band edge potential for CB/LUCO of Ag(I)-CP (40% NH₂) was about −0.50 V vs. NHE [26,75–77]. Note that, compared to the parent CP, a new state appeared in the calculated (HSE06) electronic DOS for Ag(I)-CP (40% NH₂) (Fig. 7), so it appears that the potential deduced from the calculated optical band gap directly represents the potential of the HOCO state which is calculated to be +2.40 V vs. NHE (Fig. 12). Whereas, CB and VB edges of Ag(I)-CP were calculated to be −0.30 V, and +3.45 V vs. NHE, respectively (Fig. 12). The electronic charge density plots of the mixed ligand CP (Fig. 12 and Fig. S30) supports this conclusion drawn from the DOS analysis. The majority of the electron density associated with the HOCO lies on the amine functionalized aromatic ring of the linker and is composed of the 2p orbitals of N and C. The LUCO is centred on the 2p C and O atoms present in the aromatic ring and the carboxylate group. It should be noted that there is a clear charge separation between HOCO and LUCO as the HOCO resides on the amine group of the NH₂-bdc^{2−} ligand while LUCO is centred on the non-functionalized bdc^{2−} ligand. This could explain the enhanced lifetime of the photo generated electron-hole pairs observed experimentally [24,74].

The calculated HOCO-LUCO gap of 2.8 eV is in good agreement with the experimental optical absorption threshold of 2.87 eV, meaning that photo-generated holes and electrons will be generated in the polymer at this energy. The narrow band feature suggests that, at this threshold energy, photo-generated holes will be localised on the amine groups and the associated aromatic ring while photo-generated electrons enter more de-localised states on the aromatic system of the ligands which are similar to those seen for the Ag(I)-CP. The separation of electrons and holes is an essential initial step in the photocatalytic process, the amine modification of the linker in the Ag(I)-CP, essentially creates a new state (HOCO) with a potential +2.4 V vs NHE. Hence, Ag(I)-CP (40% NH₂) can be activated using visible light. The reduction potential of benzyl alcohol (BA) to benzaldehyde (BD) is +1.9 V vs NHE and benzaldehyde (BD) to benzoic acid (BAD) is +2.5 V vs NHE [76].

Considering the bandgap structures of Ag(I)-CP (40% NH₂), it is now clear that hole (h⁺) generated in the HOCO (+2.4 V vs NHE) is more positive than that of the reduction potential of BA to BD (+1.9 V vs NHE), and it is lower than that of reduction potential of BD to BAD (+2.5 V vs NHE) leading to high selectivity in the photooxidation reaction. The CB/LUCO photogenerated electrons also have sufficient potential (−0.50 V vs NHE) to reduce the O₂ to the O₂^{•−} radical (−0.27 V vs NHE) or S₂O₈^{2−} to SO₄^{•−} (+1.44 V vs NHE) resulting in a suppression of the backward reaction [15,49,76,78]. Note that activation of persulfate by accepting an electron is more favourable than activation of O₂ as O₂ has a limited adsorption. The inorganic oxidant K₂S₂O₈ being soluble and accessible to the active sites in the catalyst can accumulate photogenerated electrons at a faster rate and promote the forward reaction, giving better yield of BD than possible with O₂. However, under such conditions the conversion of BA in presence of mixed ligand CP is lower, especially in O₂ atmosphere and it is worth noting that a limited amount of active species (O₂^{•−}/SO₄^{•−}) were generated and deactivated after two three cycle as a result of partial reduction of lattice Ag⁺ from the CP, whereas *in-situ* deposited Ag⁰ NPs in Ag@Ag(I)-CP(40% NH₂) not only promote the adsorption of oxidant (O₂/K₂S₂O₈) to the metallic sites but also enhance the light absorption efficiency. Furthermore, combining the effect of Ag NPs i.e. formation of Schottky junction with the mixed ligand Ag(I)-CP as established from

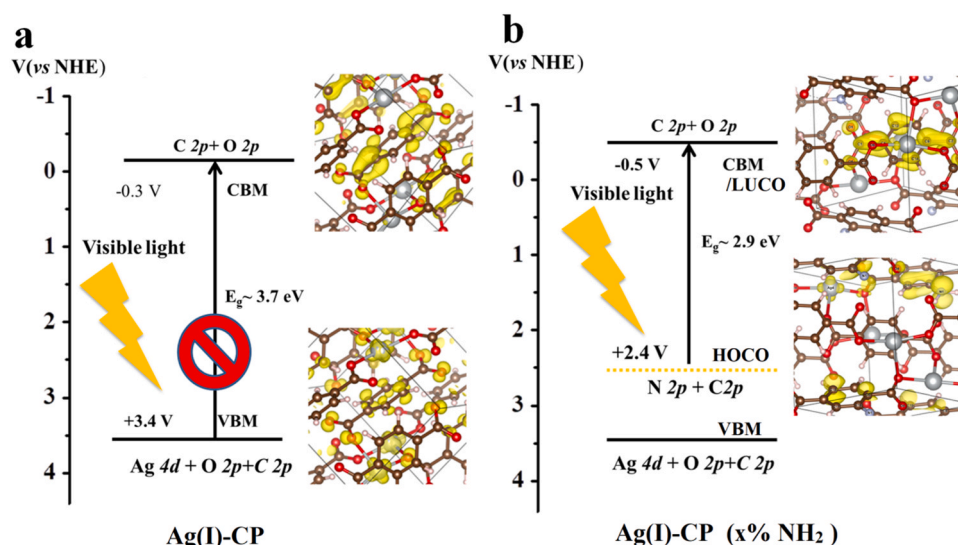
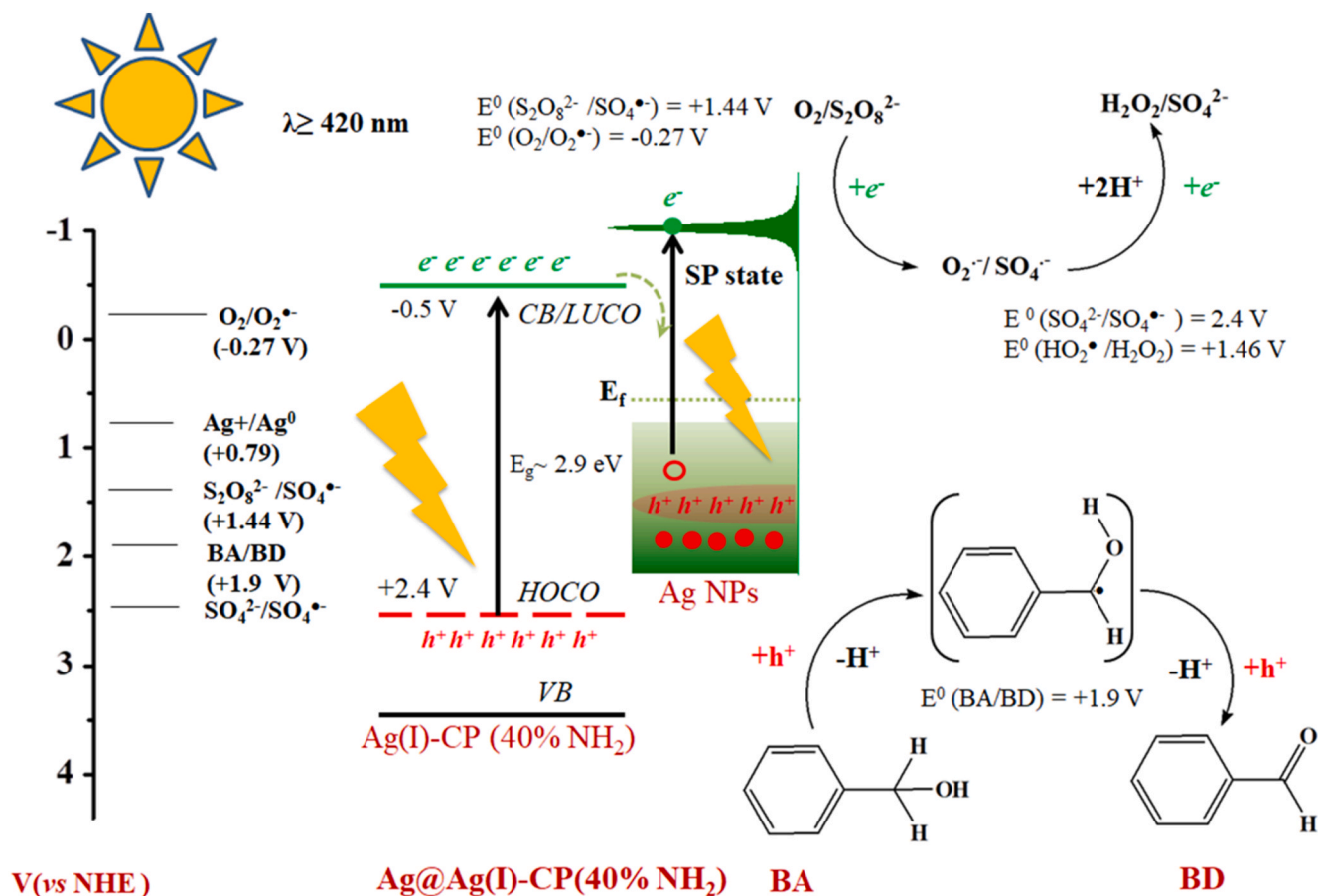


Fig. 12. Energy band structure and states of parent CP and mixed ligand CP. Inset shows the projected electron density at VBM or HOCO (bottom) and CBM/LUCO (top) of the CPs.

both theoretical and experimental results and its localized surface plasmon resonance (Scheme 2) increases the charge carrier lifetime, enhances the charge carrier density and thereby increases the rate of oxidation of benzyl alcohol while enhancing the stability of the coupled structure against reduction of Ag(I) in the CP network over multiple reuse cycles.

4. Conclusions

In summary, a new plasmonic Ag NPs coupled mixed ligand Ag(I) based coordination polymer (Ag@Ag(I)-CP (40%) NH₂) was synthesized by a one pot synthetic route. The Ag@Ag(I)-CP(40% NH₂) achieved enhanced performances toward selective BA oxidation reaction



Scheme 2. Visible light driven charge separation process in the Ag@Ag(I)-CP (40% NH₂) and generated active species responsible for the selective oxidation of benzyl alcohol (BA) to benzaldehyde (BD).

(Conversion rate of BA: $k_{K_2S_2O_8} = 38.7 \times 10^{-4} \text{ min}^{-1}$ with yield: 54.1% BD) which is about 1.4 time, 2.2 time faster compared to that of Ag(I)-CP (40% NH_2) alone, and Ag@Ag(I)-CP. This enhanced performance is obtained by the synergistic action of two counter parts Ag(I)-CP (40%) NH_2 and Ag NPs. In one side, amine functionalized ligand makes the mixed ligand CP alone a visible light active component and produces a HOCO state (+ 2.4 V vs. NHE) which is very selective to initiate hole mediated oxidation of BA to BD ($E_{\text{BA/BD}}^0 = + 1.9 \text{ V}$), whereas in another side Ag NPs (~ 6–7 nm) increases the charge carrier density and lifetime, and promotes the efficiency of adsorption/reduction of oxidants ($\text{O}_2/\text{K}_2\text{S}_2\text{O}_8$) in the coupled structure through LSPR and Schottky junction effect. Besides, the coupled structure achieved enhanced stability with respect to reuse than of their mixed ligand CP counterparts. Moreover, it would be an alternate and cheap candidate competing with Ag NPs supported system and precious Au, and Pt NPs metal based photoredox systems. Accordingly, the work represents a concrete prototype of engineering the band gap of Ag(I)-based mixed ligand CP at molecular scale and manoeuvring further its stability and visible-light absorption efficiency by *in-situ* coupling Ag NPs at nanoscale. The knowledge acquired in this study will contribute to the development of plasmonic photocatalysts for a wide range of organic transformation reactions and offer the possibility of finding suitable targeted photoredox application for advanced solar-energy conversion.

CRedit authorship contribution statement

Dr. Subrata Mandal: Synthesis of material, Methodology, Data curation, Formal analysis, Investigation, Interpretation, Writing – original draft, Writing – review & editing. **Dr. Sachin P. Nanavati:** Performed the simulation (Theoretical calculation) and related writing part, interpretation of theoretical data. **Prof. David J. Willock:** Results discussion (Theoretical and experimental): Validation of the theoretical results, Review and editing of the draft. **Prof. Rajakumar Ananthakrishnan:** Hypothesized the prime concept, Design of experiments, Supervised the execution of work, Validation of experimental data and interpretation, Upgradation of the original draft by re-writing, Overall review, editing and coordination of the manuscript as the corresponding author.

Declaration of Competing Interest

The authors declare no competing financial interest.

Acknowledgements

S.M. gratefully acknowledges the University Grant Commission (UGC), New Delhi, India for research fellowship. The authors acknowledge Department of Science and Technology (DST), India, for FESEM and PXRD facilities (at Department of Chemistry, IITKGP) and XPS facility (at Department of Physics, IITKGP). S.M. thanks Tarun Karmakar, co-researcher, for useful discussion on the experimental part. R.A. thanks to the Science and Engineering Research Board (SERB), New Delhi, India (for HPLC-PDA – Project Ref. No. SR/FT/CS-146/2011). S.P. N. acknowledges the support of the Supercomputing Wales project, which is part funded by the European Regional Development Fund (ERDF) via Welsh Government. Computing facilities for this work were provided by Supercomputing Wales (Hawk) and the ARCHER UK National Supercomputing Service via the membership of the United Kingdom's (UK) HEC Materials Chemistry Consortium, which is funded by Engineering and Physical Sciences Research Council (EPSRC, EP/L000202). This work also used the UK Materials and Molecular Modelling Hub for computational resources, MMM Hub, which is partially funded by EPSRC (EP/P020194). The collaboration that led to this research was supported in part by the seed funding in the form of a travel grant from Cardiff University's GCRF QR Funding from the Higher Education Funding Council for Wales.

Appendix A. Supporting information

Supplementary data associated with this article can be found in the online version at doi:10.1016/j.apcatb.2021.120821.

References

- [1] A. Kudo, Y. Miseki, Heterogeneous photocatalyst materials for water splitting, *Chem. Soc. Rev.* 38 (2009) 253–278.
- [2] X. Li, J. Yu, M. Jaroniec, Hierarchical photocatalysts, *Chem. Soc. Rev.* 45 (2016) 2603–2636.
- [3] A.P. Reddy, P.V. Reddy, E. Kwon, K.H. Kim, T. Akter, S. Kalagara, Recent advances in photocatalytic treatment of pollutants in aqueous media, *Environ. Int.* 91 (2016) 94–103.
- [4] C. Chen, W. Ma, J. Zhao, Semiconductor-mediated photodegradation of pollutants under visible-light irradiation, *Chem. Soc. Rev.* 39 (2010) 4206–4219.
- [5] H. Tong, S. Ouyang, Y. Bi, N. Umezawa, M. Oshikiri, J. Ye, Nano-photocatalytic materials: possibilities and challenges, *Adv. Mater.* 24 (2012) 229–251.
- [6] J.B. Pan, S. Shen, L. Chen, C.T. Au, S.F. Yin, Core-shell photoanodes for photoelectrochemical water oxidation, *Adv. Funct. Mater.* 3 (2021), 2104269.
- [7] Q.L. Zhu, Q. Xu, Metal-organic framework composites, *Chem. Soc. Rev.* 43 (2014) 5468–5512.
- [8] H. Zhang, G. Liu, L. Shi, H. Liu, T. Wang, J. Ye, Engineering coordination polymers for photocatalysis, *Nano Energy* 22 (2016) 149–168.
- [9] H.D. Xiao, J., H.L. Jiang, Metal-organic frameworks for photocatalysis and photo thermal catalysis, *Acc. Chem. Res.* 52 (2019) 356–366.
- [10] S. Kitagawa, R. Kitaura, S.I. Noro, Functional porous coordination polymers, *Angew. Chem. Int. Ed.* 43 (2004) 2334–2375.
- [11] V. Stavila, A.A. Talin, M.D. Allendorf, MOF-based electronic and optoelectronic devices, *Chem. Soc. Rev.* 43 (2014) 5994–6010.
- [12] J.B. Pan, B.H. Wang, J.B. Wang, H.Z. Ding, W. Zhou, X. Liu, J.R. Zhang, S. Shen, J. K. Guo, L. Chen, C.T. Au, L.L. Jiang, S.F. Yin, Activity and stability boosting of an oxygen-vacancy-rich BiVO_4 photoanode by NiFe-MOFs thin layer for water oxidation, *Angew. Chem. Int. Ed.* 60 (2021) 1433–1440.
- [13] M.A. Nasalevich, M. Van der Veen, F. Kapteijn, J. Gascon, Metal-organic frameworks as heterogeneous photocatalysts: advantages and challenges, *CrystEngComm* 16 (2014) 4919–4926.
- [14] F. Guo, S. Yang, Y. Liu, P. Wang, J. Huang, W.Y. Sun, Size engineering of metal-organic framework MIL-101(Cr)-Ag hybrids for photocatalytic CO_2 reduction, *ACS Catal.* 9 (2019) 8464–8470.
- [15] S. Mandal, S.P. Nanavati, D.J. Willock, R. Ananthakrishnan, Photoactive Ag(I)-based coordination polymer as a potential semiconductor for photocatalytic water splitting and environmental remediation: experimental and theoretical approach, *J. Phys. Chem. C* 123 (2019) 23940–23950.
- [16] C.H. Hendon, D. Tiana, M. Fontecave, C. Sanchez, L. D'arras, C. Sasse, L. Rozes, C.M. Draznieks, A. Walsh, Engineering the optical response of the titanium-MIL-125 metal-organic framework through ligand functionalization, *J. Am. Chem. Soc.* 135 (2013) 10942–10945.
- [17] S.M. Chavan, G.C. Shearer, S.S. Svelle, U. Olsbye, F. Bonino, J. Ethiraj, K. P. Lillerud, S. Bordiga, Synthesis and characterization of amine-functionalized mixed ligand metal-organic frameworks of UiO-66 topology, *Inorg. Chem.* 53 (2014) 9509–9515.
- [18] X.P. Wu, L. Gagliardi, D.G. Truhlar, Cerium metal-organic framework for photocatalysis, *J. Am. Chem. Soc.* 140 (2018) 7904–7912.
- [19] H. Wang, X. Yuan, Y. Wu, G. Zeng, X. Chen, L. Leng, Z. Wu, L. Jiang, H. Li, Facile synthesis of amino-functionalized titanium metal-organic frameworks and their superior visible-light photocatalytic activity for Cr(VI) reduction, *J. Hazard. Mater.* 286 (2015) 187–194.
- [20] D. Sun, L. Ye, Z. Li, Visible-light-assisted aerobic photocatalytic oxidation of amines to imines over $\text{NH}_2\text{-MIL-125(Ti)}$, *Appl. Catal. B: Environ.* 64 (2015) 428–432.
- [21] Z. Zhang, X. Li, B. Liu, Q. Zhao, G. Chen, Hexagonal microspindle of $\text{NH}_2\text{-MIL-101(Fe)}$ metal-organic frameworks with visible-light-induced photocatalytic activity for the degradation of toluene, *RSC Adv.* 6 (2016) 4289–4295.
- [22] D. Wang, R. Huang, W. Liu, D. Sun, Z. Li, Fe-Based MOFs for photocatalytic CO_2 reduction: role of coordination unsaturated sites and dual excitation pathways, *ACS Catal.* 4 (2014) 4254–4260.
- [23] L. Shi, T. Wang, H. Zhang, K. Chang, X. Meng, H. Liu, J. Ye, An amine-functionalized iron(III) metal-organic framework as efficient visible-light photocatalyst for Cr(VI) reduction, *Adv. Sci.* 2 (2015), 1500006.
- [24] X. Mu, J. Jiang, F. Chao, Y. Lou, J. Chen, Ligand modification of UiO-66 with an unusual visible light photocatalytic behaviour for RhB degradation, *Dalton Trans.* 47 (2018) 1895–1902.
- [25] L. Shen, R. Liang, M. Luo, F. Jing, L. Wu, Electronic effects of ligand substitution on metal-organic framework photocatalysts: the case study of UiO-66, *Phys. Chem. Chem. Phys.* 17 (2015) 117–121.
- [26] J. Long, S. Wang, Z. Ding, S. Wang, Y. Zhou, L. Huang, X. Wang, Amine-functionalized zirconium metal-organic framework as efficient visible light photocatalyst for aerobic organic transformations, *Chem. Commun.* 48 (2012) 11656–11658.
- [27] R. Liang, L. Shen, F. Jing, W. Wu, N. Qin, R. Lin, L. Wu, NH_2 -mediated indium metal-organic framework as a novel visible-light-driven photocatalyst for reduction of the aqueous Cr(VI), *Appl. Catal. B: Environ.* 162 (2015) 245–251.

- [28] X. Wang, S. Li, H. Yu, J. Yu, S. Liu, Ag₂O as a new visible-light photocatalyst: self-stability and high photocatalytic activity, *Chem. Eur. J.* 17 (2011) 7777–7780.
- [29] Y.P. Bi, H.Y. Hu, S.X. Ouyang, Z.B. Jiao, G.X. Lu, J.H. Ye, Selective growth of metallic Ag nanocrystals on Ag₃PO₄ submicro-cubes for photocatalytic applications, *Chem. Eur. J.* 18 (2012) 14272–14275.
- [30] X. Zhang, Y.L. Chen, R.S. Liu, D.P. Tsai, Plasmonic photocatalysis, *Rep. Prog. Phys.* 76 (2013), 046401.
- [31] P. Chen, L. Chen, Y. Zeng, F. Ding, X. Jiang, N. Liu, C.T. Au, S.F. Yin, Three-dimension hierarchical heterostructure of CdWO₄ microrods decorated with Bi₂WO₆ nanoplates for high-selectivity photocatalytic benzene hydroxylation to phenol, *Appl. Catal. B Environ.* 234 (2018) 311–317.
- [32] H. Li, F. Qin, Z. Yang, X. Cui, J. Wang, L. Zhang, New reaction pathway induced by plasmon for selective benzyl alcohol oxidation on BiOCl possessing oxygen vacancies, *J. Am. Chem. Soc.* 139 (2017) 3513–3521.
- [33] H. Göksu, H. Burhan, S.D. Mustafaov, F. Şen, Oxidation of benzyl alcohol compounds in the presence of carbon hybrid supported platinum nanoparticles (Pt@CHs) in oxygen atmosphere, *Sci. Rep.* 10 (2020) 5439.
- [34] G. Kresse, J. Furthmüller, Efficient iterative schemes for Abinitio total-energy calculations using a plane-wave basis set, *Phys. Rev. B* 54 (1996) 11169–11186.
- [35] P.E. Blochl, Projector augmented-wave method, *Phys. Rev. B* 50 (1994) 17953–17979.
- [36] J.P. Perdew, K. Burke, M. Ernzerhof, Generalized gradient approximation made simple, *Phys. Rev. Lett.* 77 (1996) 3865–3868.
- [37] J. Heyd, G.E. Scuseria, M. Ernzerhof, Hybrid functionals based on a screened coulomb potential, *J. Chem. Phys.* 118 (2003) 8207–8215.
- [38] S. Grimme, J. Antony, S. Ehrlich, H. Krieg, A consistent and accurate *ab initio* parametrization of density functional dispersion correction (DFT-D) for the 94 elements H–Pu, *J. Chem. Phys.* 132 (2010), 154104.
- [39] H.J. Monkhorst, J.D. Pack, Special points for Brillouin-Zone integrations, *Phys. Rev. B* 13 (1976) 5188–5192.
- [40] Y. Hinuma, G. Pizzi, Y. Kumagai, F. Oba, I. Tanaka, Band structure diagram paths based on crystallography, *Comput. Mater. Sci.* 128 (2017) 140–184.
- [41] M. Taddei, D. Tiana, N. Casat, J.A. van Bokhoven, B. Smit, M. Ranocchiari, Mixed-ligand UiO-66: structure–property relationships revealed by a combination of high-resolution powder X-ray diffraction and density functional theory calculations, *Phys. Chem. Chem. Phys.* 19 (2017) 1551–1559.
- [42] L. Shen, S. Liang, W. Wu, R. Liang, L. Wu, Multifunctional NH₂-mediated zirconium metal-organic framework as an efficient visible-light-driven photocatalyst for selective oxidation of alcohols and reduction of aqueous Cr(VI), *Dalton Trans.* 42 (2013) 13649–13657.
- [43] M. Kandiah, M.H. Nilsen, S. Usseglio, S. Jakobsen, U. Olsbye, M. Tilset, C. Larabi, E.A. Quadrelli, F. Bonino, K.P. Lillerud, Synthesis and stability of tagged UiO-66 Zr-MOFs, *Chem. Mater.* 22 (2010) 6632–6640.
- [44] C.D. Fast, J. Woods, J. Lentchner, T.A. Makal, Stabilizing defects in metal-organic frameworks: pendant Lewis basic sites as capping agents in UiO-66-type MOFs toward highly stable and defective porous materials, *Dalton Trans.* 48 (2019) 14696–14704.
- [45] C.M.A. Parlett, K. Wilson, A.F. Lee, Hierarchical porous materials: catalytic applications, *Chem. Soc. Rev.* 42 (2013) 3876–3893.
- [46] K.K. Yee, Y.L. Wong, Z. Xu, Bio-inspired stabilization of sulfonyl iodide RS-I in a Zr (iv)-based metal-organic framework, *Dalton Trans.* 45 (2016) 5334–5338.
- [47] W.J. Phang, H. Jo, W.R. Lee, J.H. Song, K. Yoo, B.S. Kim, C.S. Hong, Superprotonic conductivity of a UiO-66 framework functionalized with sulfonic acid groups by facile post synthetic oxidation, *Angew. Chem. Int. Ed.* 54 (2015) 5142–5146.
- [48] P. Roy, A. Schaate, P. Behrens, A. Godt, Surface-plasmon-resonance-induced photocatalysis by core-shell SiO₂@Ag NCs@Ag₃PO₄ toward water-splitting and phenol oxidation reactions, *Chem.-Eur. J.* 18 (2012) 6979–6985.
- [49] S. Mandal, R. Ananthakrishnan, Sustainable design of hierarchically porous Ag₃PO₄ microspheres through a novel natural template and their superior photooxidative capacity, *ACS Sustain. Chem. Eng.* 6 (2018) 1091–1104.
- [50] Z. Jiang, Q. Ouyang, B. Peng, Y. Zhang, L. Zan, Ag size-dependent visible-light-responsive photoactivity of Ag-TiO₂ nanostructure based on surface plasmon resonance, *J. Mater. Chem. A* 2 (2014) 19861–19866.
- [51] Z. Gu, L. Chen, B. Duan, Q. Luo, J. Liu, C. Duan, Synthesis of Au@UiO-66(NH₂) structures by small molecule-assisted nucleation for plasmon enhanced photocatalytic activity, *Chem. Commun.* 52 (2016) 116–119.
- [52] J.P. Hong, A.Y. Park, S. Lee, J. Kang, N. Shin, D.Y. Yoon, Tuning of Ag work functions by self-assembled monolayers of aromatic thiols for an efficient hole injection for solution processed triisopropylsilylthynyl pentacene organic thin film transistors, *Appl. Phys. Lett.* 92 (2008), 143311.
- [53] Y. Hou, F. Zuo, Q. Ma, C. Wang, L. Bartels, P. Peng, Ag₃PO₄ oxygen evolution photocatalyst employing synergistic action of Ag/AgBr nanoparticles and graphene sheets, *J. Phys. Chem. C* 116 (2012) 20132–20139.
- [54] W. Teng, X. Li, Q. Zhao, G. Chen, Fabrication of Ag/Ag₃PO₄/TiO₂ heterostructure photoelectrodes for efficient decomposition of 2-chlorophenol under visible light irradiation, *J. Mater. Chem. A* 1 (2013) 9060–9068.
- [55] D. Li, S.H. Yu, H.L. Jiang, From UV to near-infrared light-responsive metal-organic framework composites: plasmon and upconversion enhanced photocatalysis, *Adv. Mater.* 30 (2018), 1707377.
- [56] J.D. Xiao, L. Han, J. Luo, S.H. Yu, H.L. Jiang, Integration of plasmonic effects and Schottky junctions into metal-organic framework composites: steering charge flow for enhanced visible-light photocatalysis, *Angew. Chem. Int. Ed.* 57 (2018) 1103–1107.
- [57] S. Mao, J.W. Shi, G. Sun, D. Ma, C. He, Z. Pu, K. Song, Y. Cheng, Au nanodots@thiol-UiO66@ZnIn₂S₄ nanosheet with significantly enhanced visible-light photocatalytic H₂ evolution: the effect of different Au positions on the transfer of electron-hole pairs, *Appl. Catal. B: Environ.* 282 (2021) 119550–119560.
- [58] L. Xiong, J. Tang, Strategies and challenges on selectivity of photocatalytic oxidation of organic substances, *Adv. Energy Mater.* 11 (2021), 2003216.
- [59] H. Kim, H.Y. Yoo, S. Hong, S. Lee, S. Lee, B.S. Park, H. Park, C. Lee, J. Lee, Effects of inorganic oxidants on kinetics and mechanisms of WO₃-mediated photocatalytic degradation, *Appl. Catal. B: Environ.* 62 (2015) 515–523.
- [60] A. Tanaka, K. Hashimoto, H. Kominami, Preparation of Au/CeO₂ exhibiting strong surface plasmon resonance effective for selective or chemo selective oxidation of alcohols to aldehydes or ketones in aqueous suspensions under irradiation by green light, *J. Am. Chem. Soc.* 134 (2012) 14526–14533.
- [61] Y. Shiraishi, D. Tsukamoto, Y. Sugano, A. Shiro, S. Ichikawa, S. Tanaka, T. Hirai, Platinum nanoparticles supported on anatase titanium dioxide as highly active catalysts for aerobic oxidation under visible light irradiation, *ACS Catal.* 2 (2012) 1984–1992.
- [62] A. Tanaka, K. Hashimoto, H. Kominami, A very simple method for the preparation of Au/TiO₂ plasmonic photocatalysts working under irradiation of visible light in the range of 600–700 nm, *Chem. Commun.* 53 (2017) 4759–4762.
- [63] S. Li, J. Cai, X. Wu, F. Zheng, Sandwich-like TiO₂@ZnO-based noble metal (Ag, Au, Pt, or Pd) for better photo-oxidation performance: synergistic effect between noble metal and metal oxide phases, *Appl. Surf. Sci.* 443 (2018) 603–612.
- [64] X. Chen, Z. Zheng, X. Ke, E. Jaatinen, T. Xie, D. Wang, C. Guo, J. Zhao, H. Zhu, Supported silver nanoparticles as photocatalysts under ultraviolet and visible light irradiation, *Green Chem.* 12 (2010) 414–419.
- [65] L. Xiao, Q. Zhang, P. Chen, L. Chen, F. Ding, J. Tang, Y.J. Li, Y.C.T. Au, S.F. Yin, Copper-mediated metal-organic framework as efficient photocatalyst for the partial oxidation of aromatic alcohols under visible-light irradiation: synergism of plasmonic effect and Schottky junction, *Appl. Catal. B: Environ.* 248 (2019) 380–387.
- [66] T. Wang, X. Tao, Y. Xiao, G. Qiu, Y. Yang, B. Li, Charge separation and molecule activation promoted by Pd/MIL-125-NH₂ hybrid structures for selective oxidation reactions, *Catal. Sci. Technol.* 10 (2020) 138–146.
- [67] Z. Yang, X. Xu, X. Liang, C. Lei, Y. Cui, W. Wu, Y. Yang, Z. Zhang, Z. Lei, Construction of heterostructured MIL-125/Ag/g-C₃N₄ nanocomposite as an efficient bifunctional visible light photocatalyst for the organic oxidation and reduction reactions, *Appl. Catal. B: Environ.* 205 (2017) 42–54.
- [68] B. Liu, L. Ning, H. Zhao, C. Zhang, H. Yang, S.J. Li, Visible-light photocatalysis in Cu₂Se nanowires with exposed {111} facets and charge separation between (111) and (111) polar surfaces, *Phys. Chem. Chem. Phys.* 17 (2015) 13280–13289.
- [69] J. Guo, L. Zhang, W. Ma, T. Chen, G. Wang, N. Akram, Y. Zhang, J. Wang, Co (OH)₂-modified CuO nanoparticles enabling high-efficiency photoinduced charge transfer toward the water oxidation reaction, *Ind. Eng. Chem. Res.* 58 (2019) 22236–22243.
- [70] A. Farrokhi, M. Jafarpour, M. Alipour, Highly selective and efficient oxidation of benzylic alcohols with sulfate radical over metal-organic frameworks, *J. Organomet. Chem.* 903 (2019), 120995.
- [71] H. Jiang, P. Zhou, Y. Wang, R. Duan, C. Chen, W. Song, J. Zhao, Copper-based coordination polymer nanostructure for visible light photocatalysis, *Adv. Mater.* 28 (2016) 9776–9781.
- [72] Y. Yamakoshi, N. Umezawa, A. Ryu, K. Arakane, N. Miyata, Y. Goda, T. Masumizu, T. Nagano, Active oxygen species generated from photoexcited Fullerene (C₆₀) as potential medicines: O₂^{•−} versus ¹O₂, *J. Am. Chem. Soc.* 125 (2003) 12803–12809.
- [73] H. Zhuang, L. Yang, J. Xu, F. Li, Z. Zhang, H. Lin, J. Long, X. Wang, Robust photocatalytic H₂O₂ production by octahedral Cd₃(C₃N₃S₃)₂ coordination polymer under visible light, *Sci. Rep.* 5 (2015) 16947–16955.
- [74] M.A. Nasalevich, C.H. Hendon, J.G. Santaclara, K. Svane, B.V. Linden, S.L. Veber, M.V. Fedin, A.J. Houtepen, M.A. Van der Veen, F. Kapteijn, A. Walsch, J. Gascon, Electronic origins of photocatalytic activity in d⁰ metal organic frameworks, *Sci. Rep.* 6 (2016) 23676.
- [75] C. Zheng, G. He, X. Xiao, M. Lu, H. Zhong, X. Zuo, J. Nan, Selective photocatalytic oxidation of benzyl alcohol into benzaldehyde with high selectivity and conversion ratio over Bi₄O₅Br₂ nanoflakes under blue LED irradiation, *Appl. Catal. B: Environ.* 205 (2017) 201–210.
- [76] X. Xiao, J. Jiang, L. Zhang, Selective oxidation of benzyl alcohol into benzaldehyde over semiconductors under visible light: the case of Bi₁₂O₁₇Cl₂ nanobelts, *Appl. Catal. B: Environ.* 142–143 (2013) 487–493.
- [77] Y. Zhang, Z. Jin, Effective electron-hole separation over a controllably constructed WP/UiO-66/CdS heterojunction to achieve efficiently improved visible-light-driven photocatalytic hydrogen evolution, *Phys. Chem. Chem. Phys.* 21 (2019) 8326–8341.
- [78] D.A. Armstrong, R.E. Huie, W.H. Koppenol, S.V. Lymar, G. Merényi, P. Neta, B. Ruscic, D.M. Stanbury, S. Steenken, P. Wardman, Standard electrode potentials involving radicals in aqueous solution: inorganic radicals (IUPAC Technical Report), *Pure Appl. Chem.* 87 (2015) 1139–1150.